The effect of buoyant convection on the buoyancy-driven spreading and draining of porous media gravity currents along a permeability jump

by

Md Imran Khan

A thesis submitted in partial fulfillment of the requirements for the degree of

Master of Science

Department of Mechanical Engineering
University of Alberta

Abstract

We investigate theoretically the impact of introducing convective dissolution along the interface of a (dense) miscible gravity current propagating up- and downdip along a permeability jump in a saturated, layered porous medium. Emphasis is placed on three different dissolution scenarios, namely constant dissolution, dissolution with simultaneous shutdown and dissolution with sequential shutdown. The last two modes are book-end opposite cases that make different assumptions concerning the mixing that arises along the gravity current-ambient interface. In the case of simultaneous shutdown, all portions of the interface experience the same rate of convective dissolution. Thus the point of shutdown, the instant at which the rate of dissolution begins to decrease, is everywhere the same. Simultaneous shutdown is associated with a rapid mixing of ambient fluid contaminated through dissolution in both the horizontal and vertical directions. By contrast, and in sequential shutdown, we neglect horizontal mixing in the ambient such that, in general, the rate of dissolution depends on position. In all three dissolution scenarios, we apply a sharp interface model and consider that the permeability jump separating the upper and lower layer of the porous medium makes an angle θ to the horizontal.

To gauge the effectiveness of dissolution as a long-term trapping mechanism, e.g. for supercritical CO_2 or acid-gas, we consider the temporal evolution of the storage efficiency and examine the impact of changing the dissolution strength, the (possibly infinite) time, t_1, for the onset of shutdown and, for

$t_1 < \infty$, the e-folding decay time, t_2, which prescribes the rate at which disso-lution terminates. The along-jump distances traveled by the up- and downdip gravity currents fall as the dissolution strength increases. This observation has special importance when characterizing gravity current intermediate run-out lengths, defined (for not small t_1) as the along-jump propagation distances where there exists a balance between the fluid supplied to the gravity cur-rent vs. that lost by a combination of dissolution and basal draining. The run-out lengths so defined are classified as intermediate because, for $t > t_1$, shutdown decreases the rate of dissolution. The associated readjustment leads to a remobilization of previously-arrested gravity current fronts and the sub-sequent (though not indefinite) elongation of these along-jump flows. In turn, the distances traveled between intermediate and terminal run-out are shown to depend on the dissolution strength and t_1. Contrasting sequential vs. si-multaneous dissolution models, the former is associated with a high degree of injectate retention in the upper layer and is therefore associated with com-paratively large storage efficiencies, E_h^*. A more general comparison between dissolution models reveals regions of the parameter space where horizontal mixing in the ambient fluid plays a dynamically significant vs. minor role.

Preface

This thesis is an original work by Md Imran Khan. The mathematical formulations relating to convective dissolution in chapter 3 were designed by Md Imran Khan, with the assistance of Dr. Morris Flynn. The MATLAB code for this thesis was developed my Md Imran Khan with assistance from Dr. K.S. Bharath.

Major parts of this thesis have been submitted for publication as Khan, M.I, K.S. Bharath & Flynn, M.R. "The effect of buoyant convection on the buoyancy-driven spreading band draining of porous media gravity currents along a permeability jump", (submitted to *Transport in Porous Media*) and is currently under review. Md Imran Khan was responsible for the theoretical developments, MATLAB coding, data analysis as well as the manuscript writing. Dr. Morris Flynn was the supervisory author and was involved with concept formations and manuscript revisions.

Acknowledgements

I am deeply grateful to my academic supervisor, Dr. Morris Flynn for his insightful guidance, patience and support during my Master's program. His commitment and unwavering dedication to research have served as the biggest tokens of inspiration in my own work. It has been an absolute honor to be under his supervision in the past couple of years. He has been an excellent teacher of fluid mechanics for me and I will forever cherish the lessons I've learned and the stellar mentorship that I've received from him.

Many senior members have helped me in training to whom I am thankful for. They are Dr. Shuo Li and Dr. K.S. Bharath, who was kind enough to explain his code so that I could develop my own. Also, I am grateful to my research group mates for their constructive feedback during my presentations and a special thanks goes to the many friends that I've made in this journey here in Edmonton.

Further, I would like to extend my earnest gratitude to my loving wife, Sumaiya Farzana, who has been the absolute rock of my life and by extension, my greatest source of happiness.

Finally, I am deeply indebted to my parents who have made countless sacrifices in the pursuit of my education.

Table of Contents

List of Figures

x

List of Symbols and Definition of Terms

Nomenclature

Run-out length: Terminal horizontal distance travelled by the gravity current

Run-out time: Time taken to cover run-out length

Shutdown: Decay in the dissolution rate as a result of upper layer saturation

Latin

f_a Downdip volume fraction

k Permeability

L_N^* Non-dimensional run-out length

Pe Péclet number

q_d Volumetric rate of convective dissolution per unit area of fluid-fluid interface

t_{95}^* Time (non-dimensional) taken to reach 95% of terminal run-out

t_0 Onset time for convective dissolution

t_1 Time for which the dissolution rate is constant

t_2 e-folding decay time for the dissolution shutdown regime

w_{drain} Draining velocity

x_N Nose position

Greek

ϕ Porosity

Chapter 1

Introduction

1.1 Motivation

The level of carbon dioxide (CO_2) in the air has risen on average from 315 ppm measured in 1960 to 408.53 ppm measured today and is estimated to rise to 450 ppm by 2040. From data gathered from air trapped in ice cores in Antarctica, it was reported that the lowest carbon dioxide concentration 650,000 years and 750,000 years before present was 170 ppm (Lüthi et al. 2008). In 2018 alone, it was estimated that fossil-fuel related emissions of CO_2 hit a record high 37.1 billion metric tons. To make matters worse, the average global temperature at the Earth's surface albeit with some variation has closely followed this rising trend of average CO_2 concentration: varying from roughly 9°C colder than present day readings to 6°C hotter (Lüthi et al. 2008). Following suit with rising global temperatures, sea levels are also projected to increase and this in conjunction with the emission of unsustainable amounts of CO_2 to the atmosphere, is leading towards catastrophe. However, the rising trend of temperature shows greater fluctuations than CO_2 concentrations and has generally increased by 0.8°C in the last 150 years (Huppert and Neufeld 2014).

The atmosphere's most abundant of gases namely nitrogen and oxygen do not contribute to global warming. However, this cannot be said in the cases of water vapor, methane and CO_2, which combined constitute the majority

of the greenhouse effect (Huppert and Neufeld 2014). Although methane is 70 times more potent per unit mass than CO_2 in the absorption of infrared radiation that is reflected from the Earth's surface, its effectiveness declines quickly. Currently, the largest sources of methane pollution to the atmosphere is through wetlands and cattle (Khalil and Shearer 2000). However, the extent of methane emissions (0.6 gigatons per year) is small when faced with the 34.81 gigatons per year annual addition of CO_2 from anthropogenic sources (Tiseo n.d.) measured in 2020.

Globally, 25% of the world's energy use is derived from burning of the conventional fossil fuels like natural gas and coal in stationary sources like power plants with activities from industrial processes and motorized transport contributing 20% and 13%, respectively (Huppert and Neufeld 2014). These activities when combined release a tremendous amount of pollutant gases like CO_2 into the atmosphere. Any additional contribution of CO_2 into the atmosphere could result in severe damage to the atmosphere.

The residence time, τ of CO_2 in the atmosphere is stated in the initial 1990 IPCC Climate report to be in the range of 50 to 200 years (Essenhigh 2009). Given this large value of τ, it is generally concluded among many researchers that CO_2 emissions from burning fossil fuels should be curbed. Recognizing that there are limits (economic and otherwise) to the amount of reduction, remediation efforts are also be considered. An example of one such remediation effort is geoengineering. This is defined as the intentional large scale manipulation of the Earth's climate, aimed at maintaining a desired environmental condition against changes made by perturbations, either natural or from human activities (Keith 2000). Extreme applications of geoengineering to limit additional warming of the Earth's atmosphere include the installation of space mirrors to reflect and scatter incoming solar radiation. However, these approaches are extremely controversial and might result in irrevocable
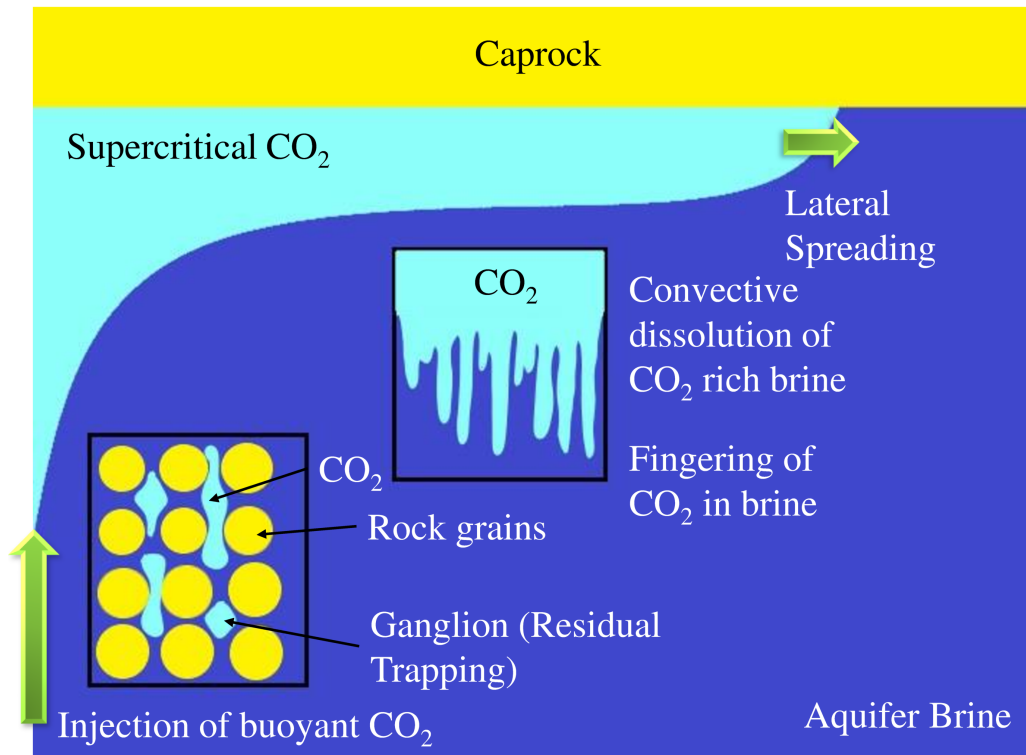
Figure 1.1: Overview of residual and convective dissolution trapping in the geological sequestration of CO_2 and the associated fluid mechananics namely: buoyancy driven spreading and dissolution of CO_2 in aquifer brine

damage to the Earth (Keith 2000). Further, the definition of geoengineering is still ambiguous and the solutions that include low-mass space-based scattering systems for altering the planetary albedo (Keith 2000) and the addition of sulfur dixoide to the Earth's atmosphere does not address the need for large scale CO_2 mitigation.

A less controversial (though not yet fully accepted) solution is to sequester or capture the CO2 generated e.g. by stationary sources. Indeed, the 2018 IPCC report concludes that, approximately 5 gigatons of CO_2 should be sequestered using Carbon Capture and Storage (CCS) technology in order to cap the rate of global temperature rise to 1.5°C/year (Allen et al. 2018). Possible injection sites include depleted oil and gas reservoirs, empty coal seams and

deep saline aquifers. Of the three, saline aquifers have the most voluminous storage capacities (Huppert and Neufeld 2014).

When the CO_2 is injected below a depth of 800 m, it becomes supercritical with an average density of about $600 \, \text{kg/m}^3$. In this state, CO_2 behaves like a liquid and thus its dynamics can be modelled with fluid mechanics (Huppert and Neufeld 2014). Nordbotten et al. (2005) examined the characteristics of brine and supercritical CO_2 in aquifers where surface temperatures vary from 10 to 20°C, with temperature gradients that fall in the range 25 to 45°C/km. In shallow aquifers located at depths of 1000 m below sea level, the sc-CO_2 density lies in the range 266 to 714 kg m^{-3}. Correspondingly the density of brine, which a function of the saline concentration in addition to temperature, lies in the range 998 to 1230 kg m^{-3}. In contrast, deep aquifers, envisaged at 3000 m below sea level have a sc-CO_2 density between 470 to 733 kg m^{-3} and brine density in the range 945 to 1202 kg m^{-3}. Additionally, the viscosity of sc-CO_2 varies between 0.023 to 0.0611 mPa·s while the viscosity of brine lies in the range of 0.195 to 1.58 mPa·s. This leads to a mobility ratio of 0.026-0.22 between the sc-CO_2 and brine.

This section will summarise the behavior of CO_2 at supercritical states: namely flow models that capture the essential dynamics, the containment and leakage mechanisms of CO_2 and the trapping mechanisms (residual trapping, minearilization, and convective dissolution) exploited to keep the CO_2 sequestered below ground. The associated fluid mechanics are illustrated in fig. 1.1. With brine densities ranging between 945 and 1,202 kg/m^3 at these depths where temperature gradients can reach a maximum value of $45°C km^{-1}$ (Huppert and Neufeld 2014), the density contrast between sequestered CO_2 and ambient brine is large and this gives rise to buoyant plumes of injected CO_2 which must be arrested by impermeable cap rocks and the aforementioned mechanisms of trapping.

Residual trapping which results from capillary snap-off of the CO_2 phase is parameterized through multiphase flow models.. These models incorporate the effect of surface tension by considering changes in relative permeability of both phases and the effective porosity (Huppert and Neufeld 2014). Capillary forces are expressed using the Bond number, $B = (\Delta \rho g L_H)/p_e$ where L_H is the unconfined aquifer length scale and p_e is the capillary pressure for CO_2 breakthrough. To capture the combined effect of permeability ratio, injection pressure and temperature, the gravity number, $N_{gv} = (k_v L \Delta \rho g)/(Hu\mu_{brine})$ is used (Ide et al. 2007). Here u is the average Darcy velocity, L is the defined as the length of the aquifer, H is the height of the aquifer, μ_{brine} is the dynamic viscosity of the aquifer brine, and $\Delta \rho$ is the density difference. Analytical studies (Kochina et al. 1983) of gravity currents comprised of CO_2 through brine saturated strata used similarity analysis to model the evolution of the volume and the nose extent, $x_N \propto t^\beta$ where the exponent is obtained by resolving an eigenvalue problem. The simulation results (see Figure 3 in Ide et al. (2007)) show that the addition of capillary pressure to flow models of CO_2 in porous aquifers and the presence of a finite aquifer inclination results in a higher fraction of CO_2 trapped. The latter is explained by the fact that residual trapping is driven by migration which exposes larger areas for trapping of saturated CO_2. Furthermore, a downward trend of injected gas trapped is obtained for high values of N_{gv}. The results further reveal that brine imbibition immediately after injection of CO_2 considerably increased the amount of trapping. Based on these studies, an advanced approach (Qi et al. 2009) to increase storage efficiency involves injecting chase brine immediately after the injection of CO_2. This leaves over 90% of the CO_2 trapped as immobile pore scale droplets. In addition to a reduced need of constant monitoring, the method does not depend on cap to contain CO_2 and the presence of favourable mobility ratios, defined as the ratio of the viscosity of injected

fluid to displaced fluid enables a more uniform sweep of the aquifer leading to higher storage efficiencies.

The other form of curbing atmospheric emissions highlighted in figure 1.1 is through convective dissolution, which is a prospective long-term trapping mechanism of sequestering CO_2 in saline aquifers since the CO_2 once dissolved remains permanently trapped. The modelling problem is nuanced since it involves the interaction of three phases namely: ambient fluid phase, super-critical CO_2 phase and the porous media phase. The supercritical CO_2 is less dense than the ambient brine and so rises as a buoyant plume. In addition, CO_2 partially dissolves in the brine and this might trigger convective or fingering instabilities. The instabilities are triggered when the porous media Rayleigh number of the boundary layer $Ra_{bl} = Ra\delta/H$, exceeds a critical value, Ra_c (Huppert and Neufeld 2014). Here $Ra = (g\Delta\rho_c KH)/(\mu_w \phi D)$ where K is the permeability of the medium, H is the aquifer depth, ϕ is the porosity, D is the diffusivity of CO_2 in water and $\Delta\rho_c$ is the density difference between the ambient and CO_2-saturated brine. Fingers may appear anywhere between 10 days and 2000 years (Huppert and Neufeld 2014). The Nusselt number ($Nu = F_c H/\phi D\Delta C$), the non-dimensional equivalent of convective flux F_c, is used to evaluate the efficacy of the fingers in removing CO_2 from the gravity current. Here ΔC is the difference in concentration between CO_2-staurated water and the ambient.

Various pilot and full scale studies into the geological sequestration of CO_2 have already been started and have shown appreciable progress over the years. Perhaps the best studied CO_2 injection site is the Sleipner project located in the North Sea. Here, supercritical CO_2 (sc-CO_2) has been sequestered at a depth of 1 km below the sea bed at a rate of 1 Mt/year since 1996 (Huppert and Neufeld 2014). Other notable projects include the In Salaah injection site in Algeria and an injection project in Weyburn, Canada where the CO_2 is

used for enhanced oil recovery (EOR). With large scale sequestration of CO_2 into subsurface reservoirs and brine filled aquifers, the geomechanical response of reservoirs to supercritical CO_2 needs be considered. The large volumes of fluid injected into the subsurface at critically stressed regions of the Earth's crust can induce seismic activity (Zoback and Gorelick 2012). Key concerns from a fluid dynamics standpoint include the type of leakage associated with seismicity, how the pressure field varies with reservoir properties and geometric heterogeneities and the possibility of monitoring and controlling aquifer pressure (Huppert and Neufeld 2014). For instance, interferometric synthetic aperture radar (InSAR) data from three injection wells at the previously mentioned In Salaah CO_2 sequestration site in Algeria show an average of 1.5 cm of vertical uplift of the desert floor (Rinaldi et al. 2015). Besides the geomechanical ramifications, the issue of cost also needs to be considered. The cost of trapping CO_2 beneath the subsurface is influenced largely by the capture and storage cost. For instance, in the design of the CO_2 storage system employing residual trapping using chase brine injection (Qi et al. 2009), it is approximated that 4×10^{-7} kg of CO_2 is produced when 1 kg of brine is injected which is considerably less than the amount of CO_2 trapped ($< 0.0001\%$) (Qi et al. 2009). Capital costs largely include the setting up of wells, pumps, transport systems and injection parts. Moreover, the associated sunk costs are but a small fraction of the entire project cost ($< 3\%$) (Leonenko and Keith 2008).

For these and other projects, besides the financial concerns associated with initial start-up, migration (particularly vertical migration) poses a risk that injectate may return to the surface. Within a heterogeneous formation or a reservoir already punctured by multiple injection and production wells, there exists some likelihood that leakage might occur through isolated fissures, cap rock edges, or old, poorly-sealed boreholes. As the sc-CO_2 spreads by buoyancy over long lateral distances, it continuously samples the underside of the cap

rock for possible leakage pathways. To this end, a variety of studies have been conducted considering confined (Nordbotten and Celia 2006; Zhao and Ioannidis 2007) vs. unconfined layers (Pritchard 2007). In the latter case especially, the rate of leakage increases with the gravity current thickness. Thus, more leakage is associated with lower overall storage efficiencies though the precise details are obviously a strong function of the geometric properties of the formation.

The other possibility is that injectate leakage is distributed. In the large Bond number limit, this problem has been investigated by, among others, Goda and Sato (2011), Sahu and Flynn (2015) and Bharath et al. (2020). Goda and Sato (2011) and Bharath et al. (2020) assume that high- and low-permeability layers are infinite in vertical extent. Key to their analysis is to quantify the run-out length, defined as the terminal horizontal distance travelled by the gravity current. When run-out is achieved, the influx to the gravity current balances draining via leakage. Run-out lengths can also be defined when the depth of the low permeability layer is finite. Here, however, run-out is later followed by a remobilization of the (primary) gravity current as a result of the formation and propagation of secondary gravity currents along the (impermeable) boundaries characterizing the low permeability layer (Bharath and Flynn 2021). In the present study, we examine a complementary problem and make the high- rather than the low-permeability layer of finite thickness. Making this change does not directly alter the draining dynamics but it is crucially important when one considers the additional influence of convective dissolution. To this end, we demonstrate below that the variation of convective dissolution with time, t, provides a second, independent mechanism by which a previously arrested gravity current front may become remobilized.

Convective dissolution was studied experimentally by MacMinn and Juanes (2013) in a sloping Hele Shaw cell with an impermeable upper boundary. They

found that the updip migration of the buoyant injectate was halted as a result of convective dissolution and the formation and vertical propagation of (comparatively dense) fingers resulting from the mixing of the injectate and the ambient fluid. Szulczewski et al. (2013) extended MacMinn and Juanes (2013) by categorizing the different dissolution regimes of which they counted seven, i.e. early diffusion, fingering, shutdown/fingering, shutdown/slumping, shutdown/Taylor slumping, Taylor slumping, and finally late diffusion. In the fingering stage, the rate of convective dissolution is constant because the fingers descend at a constant speed. As the fingers strike the bottom boundary, a layer of contaminated fluid begins to accumulate. Eventually, the thickness of this layer becomes large enough to arrest convective dissolution. Therefore, and as the ambient becomes saturated with contaminated fluid, the rate of dissolution asymptotically reaches zero. In the long term the effectiveness of the dissolution depends on the depth of the lower layer of the aquifer. If the aquifer depth is small, shutdown will initiate early on and the fraction of the injectate that is dissolved will diminish quickly. This will limit the long-term storage efficiency which will drop quickly on account of the dissolution being switched off. Hence by integrating various regimes of dissolution, the identification and selection of favourable locations for sequestering CO_2 can be accomplished.

Despite the inherent complexity of the different regimes of convective dissolution, the overall process can be parameterized according to figure 1 (MacMinn et al. 2011). In this figure, t_0 signifies a delay time during which are established the hydrodynamic instabilities that feed finger growth. The constant dissolution regime characterized by the time t_1 corresponds to fingers falling at a constant velocity. When $t = t_0 + t_1$, dissolution begins to slow because the fingers make contact with an impermeable boundary. Thereafter, fluid discharged by the fingers ascends as a curtain of dissolved fluid, depressing
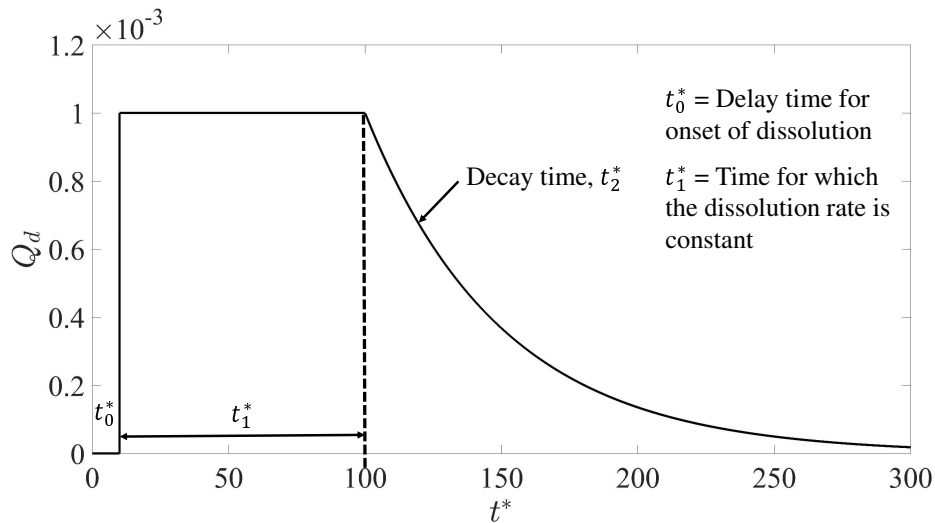
Figure 1.2: Time variation of the convective dissolution rate, Q_d; Q_d is defined mathematically by (3.20).

the dissolution rate. The time $t = t_0 + t_1$ represents the onset of the so-called shutdown regime, a regime during which the rate of dissolution decreases with an e-folding time t_2.

1.2 Thesis Objectives

In light of all of the above, we propose to explore, theoretically, the complicated interplay between injectate up- vs. downdip spreading, draining and dissolution. Thereby, our work simultaneously extends MacMinn and Juanes (2013) (spreading and dissolution but no draining) and Bharath et al. (2020) (spreading and draining but no dissolution). In so doing, we shall refer to the flow depicted schematically in figure 1.3, which situates a (discrete) source some vertical distance away from an inclined permeability jump. Here, and in contrast to Goda and Sato (2011), MacMinn and Juanes (2013) and Szulczewski et al. (2013), we assume a dense rather than a buoyant injectate. This choice is made for mathematical convenience and also to make our anal-
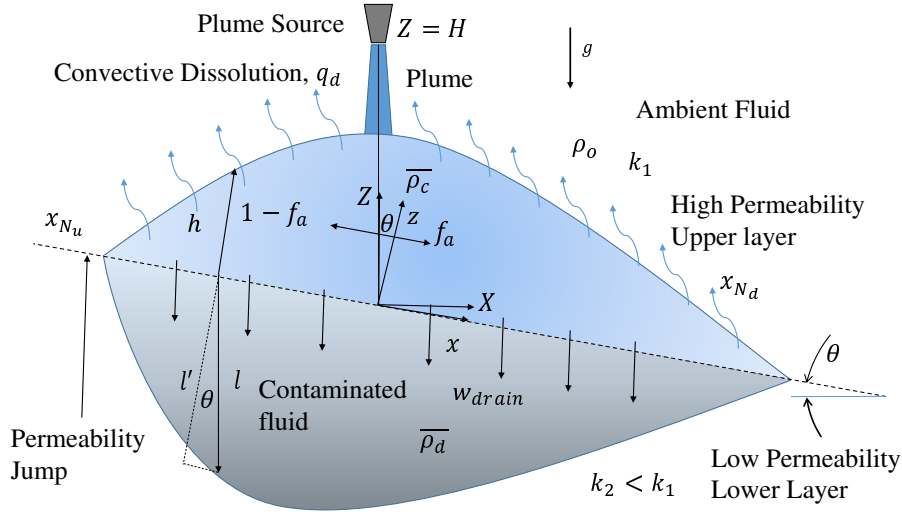
Figure 1.3: [Color online] Schematic showing the spatial-temporal evolution of discharged plume fluid in the up- and downdip directions along the permeability jump. Also illustrated are dissolution and draining. Here, the vertical dimension of the up- and downdip gravity currents has been exaggerated for emphasis and clarity.

ysis consistent with select seminal works on gravity currents in porous media e.g. Huppert and Woods (1995), Vella and Huppert (2006), and Lyle et al. (2005). Note, however, that the choice of orientation is immaterial provided that density contrasts are small so that the Boussinesq approximation applies.

In performing our analysis, reference will be made to two different shutdown modes, one local and the other global. In the latter case, we assume that contaminated fluid propagates with relative ease through the ambient in the upper layer. Therefore, in the space above the up- and downdip gravity currents, concentration gradients are relatively weak (see figure 1 of Bolster (2014)) suggesting that all points along the exposed upper surface of the gravity currents begin to experience shutdown at the same time. We refer to this scenario as simultaneous shutdown. At the bookend opposite extreme is a case where the lateral motion of contaminated fluid is slow. Here, different portions of the gravity current surface experience contaminated fluid having different

concentrations of the injectate. Shutdown is therefore experienced at different times with those regions proximal to the source shutting down well before those regions further away from the source. This latter scenario is referred to as the sequential shutdown regime. Neither of the simultaneous or sequential descriptions is strictly correct. However, the solutions afforded by these two limiting cases must bound the true solution. In regions where the bound is tight we therefore enjoy good insights into the true nature of the flow.

1.3 Thesis Outline

In this thesis, we utilize theory to address the knowledge gaps outlined in section 1.2. The rest of this thesis is organized as follows. In chapter 3, we incorporate into the theoretical equations of the flow just described, a means of superposing convective dissolution (including the possibility of simultaneous or sequential shutdown) and predict both the transient and steady state solutions as the gravity current migrates along the inclined permeability jump. In section 4.1, we study the effect of the dissolution strength assuming constant dissolution, and consider the significance of a deep upper layer on the storage and runout. Here, a prolonged injection period is considered with a constant flux output. The key aspects such as the (i) the influence of dissolution strength on the dynamics of the gravity current in the upper layer, (ii) priority between up- and downdip asymmetry (iii) storage as a function of dissolution strength and inclination angle of the permeability jump (iv) differences between up- vs. downdip runout lengths due to asymmetric volume fractions are the highlights of this section.

Sections 4.2 and 4.3 respectively consider simultaneous and sequential shutdown and examine the influence of e.g. t_1, t_2 and the permeability jump angle on the dynamics of the flow. Specifically, we quantify the time taken to reach 95% of the runout length in the $t_1 - \theta$ parameter space and likewise in the

domain of $t_2 - \theta$.

In chapter 5, we extend the study of gravity current in shallow layers whilst having a steady source and predict the dynamics for short term injection in shallow layers. For this, we modify the source influx boundary conditions used in chapter 3 and explore the transient dynamics of the gravity current with particular emphasis on the post-injection phase. Model results that calculate the time taken for the gravity current to fully dissppear from the upper layer and the maximum distance traversed before source influx curtailment are then displayed as functions of t_1 and θ. The pattern of flow behavior for unsteady sources forms a key observation of this study

Building on the results from chapter 5, we investigate in chapter 6 the regions of the parameter space considered where the solutions from simulatneous vs. sequential shutdown are similar and where they are radically different. In doing so, the regions observed allow us to target conditions for similar flow dynamics, thus enabling us to uncover the true nature of the flow from the two dissimilar regimes of shutdown.

In chapter 7, we summarize key conclusions and present avenues for future work.

Several parts of this thesis have been submitted for as Khan, M.I, K.S. Bharath & Flynn, M.R. The effect of buoyant convection on the buoyancy-driven spreading band draining of porous media gravity currents along a permeability jump. (submitted to *Transport in Porous Media*) and is currently under review. The results have been presented in the IGR Symposium organised by the Department of Physics at the University of Alberta on November 2020. Additionally, parts of this thesis have been presented in the Interpore 2020 conference held online.

Chapter 2

Review of porous media gravity currents

2.1 Flow along an impermeable bottom boundary

In outlining the objectives for this thesis, reference was made to the complicated interplay between dissolution, advection and draining. While it remains to present and discuss the associated governing equations, it is instructive to consider, for illustrative purposes, the less cumbersome problem of a gravity current that propagates through a porous medium without experiencing either draining or dissolution. Once the associated dynamics are well understood, the business of adding additional terms to account for other effects becomes more straightforward. To this end, this chapter presents an analysis of a porous media gravity current traveling down an impermeable, sloping boundary. Throughout, we follow the derivation presented by Huppert and Woods (1995) and therefore consider a gravity current fed by an isolated source located along the boundary – see fig. 2.1.

Our analysis begins by considering the mass continuity equation, which is written as:

$$\nabla \cdot u = 0 \tag{2.1}$$

Darcy's law is then used to obtain the equation of motion along the slope
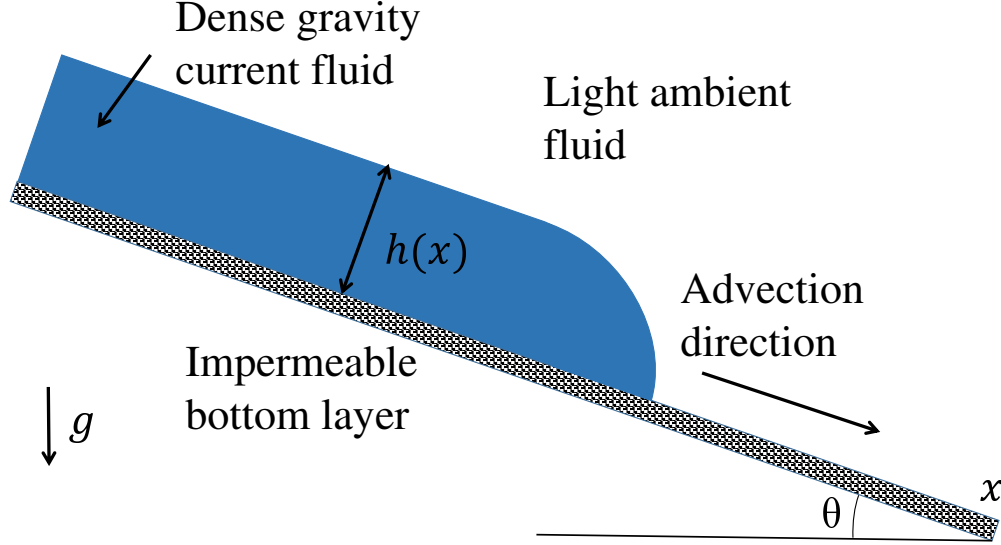
Figure 2.1: Schematic of a gravity current propagating through a sloping porous layer with an impermeable bottom boundary.

(Bear 1988; Phillips 1991) which is given as:

$$\boldsymbol{u} = -\frac{k(\phi)}{\mu}[\nabla P + \rho g(-\sin\theta, \cos\theta)] \tag{2.2}$$

Here, μ is the dynamic viscosity, g is the acceleration due to gravity and ρ is the density of the gravity current, and finally k is defined as the permeability which is a function of the porosity, ϕ, The porosity is the ability of a medium to transmit fluid. k also depends on the interconnection of the pores and on the average grain size.

The pressure variation within the gravity current fluid is hydrostatic in nature and is thus given by:

$$P(x, y, t) = -g\cos\theta\Delta\rho y + p(x, t) \tag{2.3}$$

where ρ is the excess density of the gravity current over the surrounding ambient. In addition, the hydrostatic pressure, $p(x, t)$ along the slope is defined as:

$$p(x, t) = (\rho - \Delta\rho)gx\sin\theta + \Delta\rho gh(x, t)\cos\theta + P_1 \tag{2.4}$$

15

Here, P_1 is a constant. Using Darcy's law from 2.2, the alongslope velocity as derived by Huppert and Woods (1995) is given as:

$$u(x, y, t) = -\frac{k(\phi)}{\mu}\Delta\rho g\left(\frac{\partial h}{\partial x}\cos\theta - \sin\theta\right) \tag{2.5}$$

The depth averaged continuity equation (Huppert and Woods 1995) for the flow is given as follows:

$$\frac{\partial}{\partial x}\left[\int_0^{h(x,t)} u(x, y, t)\, dy\right] = -\phi(h)\frac{\partial h}{\partial t} \tag{2.6}$$

Inserting eq. (2.5) into eq. (2.6), we get the integral form of the governing equation to solve for the gravity current thickness:

$$\frac{g\Delta\rho}{\mu}\frac{\partial}{\partial x}\left[\left(\frac{\partial h}{\partial x}\cos\theta - \sin\theta\right)\int_0^{h(x,t)} k(\phi)\, dy\right] = \phi(h)\frac{\partial h}{\partial t} \tag{2.7}$$

which is subject to the following global mass balance:

$$\int_0^{L(t)} dx\left(\int_0^{h(x,t)} \phi(y)\, dy\right) = \int_0^t q(t')\, dt' = V(t) \tag{2.8}$$

Here L is the horizontal extent of the gravity current, $V(t)$ is the volume of the dense fluid at time t and $q(t)$ is the source volume flux. k, which is a function of the porosity can typically be expressed as:

$$k(\phi) = k_0\phi^n \tag{2.9}$$

where n lies between 2 and 3 in natural rocks (Phillips 1991). Also, k_0 which scales as the square of the mean grain diameter is determined experimentally and is found from the Kozeny-Carman equation, which is given as

$$k_{i,0} = \frac{d_{i,0}^2}{180(1 - \phi)^2} \tag{2.10}$$

(Dullien 2012). Here $i = 1, 2$ and $d_{i,0}$ is the mean grain diameter. Another predictive model for permeability is presented in Rumpf and Gupte (1975) which is given as follows:

$$k = \frac{\phi^{5.5} d^2}{5.6} \tag{2.11}$$

Huppert and Woods (1995) made the assumption that the porosity varies linearly in a direction perpendicular to the boundary such that:

$$\phi = \phi_0 + \phi_1 y \tag{2.12}$$

Inserting this last expression in (2.7) with ϕ_0 being non-zero, we get:

$$R \frac{\partial}{\partial x}\left[\left(\left(1 + \frac{\phi_1 h}{\phi_0}\right)^{n+1} - 1\right)\left(\frac{\partial h}{\partial x}\cos\theta - \sin\theta\right)\right] = \left(1 + \frac{\phi_1 h}{\phi_0}\right)\frac{\partial h}{\partial x} \tag{2.13}$$

Here, $R = \phi_0^n \Delta\rho g k_0 / [\phi_1(n+1)\mu]$. Likewise the global mass conservation equation can be reduced to:

$$\int_0^{L(t)} \frac{(\phi_0 + \phi_1 h)^2 - \phi_0^2}{2\phi_1}\, dx = Q(t) \tag{2.14}$$

As the gravity current migrates outward on the impermeable bottom boundary, it becomes long and thin and thus the ration $\phi_1 h / \phi_0$ becomes negligible, implying that the porosity across the current is constant. Thereafter, Huppert and Woods (1995) derived a non-linear advection equation to calculate the temporal evolution of the gravity height, $h(x,t)$ while assuming that the upper layer is sufficiently deep that any secondary motion induced by the current is negligible.

$$\phi \frac{\partial h}{\partial t} = \frac{kg'}{\nu}\left[\frac{\partial}{\partial x}\left(h\frac{\partial h}{\partial x}\right)\cos\theta - \frac{\partial h}{\partial x}\sin\theta\right] \tag{2.15}$$

Here, the reduced gravity, g' is defined as $g' = g\Delta\rho/\rho$. Equation 2.15 shows that as the gravity current elongates, h gets progressively smaller, causing the gravity current to become long and thin. Also, the equation is based on the assumption that the interface between the gravity current and the ambient is sharp. Similar equations for an axisymmetric gravity current were later derived by Lyle et al. (2005), where the authors demonstrated that in the case of a constant flux source, the areal extent of the gravity current is directly

proportional to $t^{2/3}$ for a two dimensional rectangular geometry while it varies as $t^{1/2}$ for a an axisymmetric one.

2.2   Flow along a permeable bottom boundary

By making the bottom boundary permeable to source fluid, leakage or drainage through the bottom boundary takes place. The source fluid is now divided between advection which takes places along the top surface of the permeable boundary vs. leakage that occurs across the boundary. From early studies that were conducted in this configuration, drainage was modelled as either a point sink or fissure (Farcas and Woods 2013a) or as a local line sink (Neufeld et al. 2009; Neufeld et al. 2011). Distributed leakage was modelled by Pritchard et al. (2001) and Neufeld and Huppert (2009),Woods and Farcas (2009),Yu et al. (2017),Farcas and Woods (2013b) and Bharath et al. (2020). By including leakage, the governing equation for the gravity current thickness, h, becomes

$$\phi\frac{\partial h}{\partial t} = \frac{kg'}{\nu}\left[\frac{\partial}{\partial x}\left(h\frac{\partial h}{\partial x}\right)\cos\theta - \frac{\partial h}{\partial x}\sin\theta\right] - w_{\text{drain}} \tag{2.16}$$

Here, w_{drain} is the draining velocity of the source fluid leaking into the lower layer of the model configuration. In the present study, the primary focal point of leakage through the draining boundary will be that of distributed leakage. This form of leakage was investigated in early work by Pritchard et al. (2001) along a horizontal permeability jump, where the permeability of the draining layer is considered to be very small in comparison to the permeability of the upper layer. Additionally the depth of the draining layer is taken to be small as well. Hence the draining velocity is given as follows:

$$w_{\text{drain}} = \frac{k_2 g'}{\nu}\left(\frac{h}{b}\right) \tag{2.17}$$

Here, b is defined as the depth of the draining layer. Model results from Pritchard et al. (2001) predict that as the influx to the gravity current bal-

ances the draining at its base in its steady state, a finite *runout* distance is reached. In work the followed, Goda and Sato (2011) also considered a horizontal permeability jump, modelled a deep draining layer of semi-infinite thickness in contrast to a shallow layer. In their work, the authors derived an equation for the draining layer velocity which is as follows:

$$w_{\text{drain}} = \frac{k_2 g'}{\nu}\Big(1 + \frac{h}{l}\Big) \tag{2.18}$$

where l is defined as the transient draining layer depth. In the long term limit as l becomes very large such that $h/l \ll 1$, $w_{\text{drain}} \to k_2 g'/\nu$. This is termed as the steady state draining velocity and is similar to the predictions made by Pritchard et al. (2001). After reaching a steady state draining velocity, the gravity current migrating along the horizontal permeable boundary comes to a halt as the rate of basal outlfux matches the source influx and the gravity current at this point has been said to traverse a finite runout length. Both Pritchard et al. (2001) and Goda and Sato (2011) consider a zero entrainment condition in the draining fluid, which leads to the gravity current and the draining fluid having the same value for the reduced gravity.

Simulations involving inclinded boundaries were conducted by Vella and Huppert (2006) and De Loubens and Ramakrishnan (2011). In theses studies, the boundary is considered to be impermeable. In contrast, recent investigations considering inclined permeability jumps with permeable lower boundaries have been carried out by Bharath et al. (2020) and Bharath and Flynn (2021) in which the draining layer is taken to be deep in vertical extent. In current study, we limit our focus to deep draining layers of semi infinite thickness as opposed to a thin, permeable draining boundary as in Woods and Farcas (2009) and Farcas and Woods (2009), where the authors have additionally considered capillary entry pressure and the effect of drainage on capillary retention of CO_2 in a layered permeable rock.

2.3 Layered Porous Formations

The study of density driven flows in porous media with a constant permeability has been investigated by numerous researchers (Sahu and Flynn 2015; Vella and Huppert 2006; Lyle et al. 2005) in the past. However, this is an idealized scenario which differs in large extents when compared to the actual configurations found within porous rocks. In a realistic scenario, there exits multiple layers of different permeabilities within geological formations that can be modelled theoretically by the addition of deep or shallow layers in the model configuration. This provides a means to simplify large scale heterogeneities found in typical reservoirs which vary in depth between 1 and 10 m (Cowton et al. 2016). In sedimentary formations, the presence of multiple layers is rather ubiquitous. Pritchard et al. (2001) studied the advection of dense gravity current fluid across a horizontal permeable layer, which is separated from a thin underlying layer of very low permeability. Their analytical results in both planar and axisymmetric geometries predict that at early times, the motion of the gravity current follows a self similar solution but as the draining to the underlying regions matures, the velocity of the gravity current in the upper layer falls and it ultimately gets arrested before being fully drained into the lower layer. A complementary experimental investigation involving planar gravity currents is also carried out by Pritchard et al. (2001) which supports their theoretical model. Following this last publication, several investigations involving the addition of a thin layer beneath the gravity current layer have been carried out (Neufeld and Huppert 2009; Woods and Farcas 2009; Yu et al. 2017; Hewitt et al. 2020). By contrast, the study of gravity current dynamics and storage by adding layers of deep vertical extent is far less prevalent. We have previously mentioned that Goda and Sato (2011) and Sahu and Flynn (2017) have considered a deep lower layer, through which the gravity current

drains to the underlying ambient. Goda and Sato (2011) consider two injection modes namely: a constant flux release and a finite volume release and study the associated dynamics with capillary retention combined. The solutions depend on the permeability ratios and injection times considered in Goda and Sato (2011) and are generally considered to be unique in each case.

Chapter 3

Mathematical Model

3.1 Problem Definition and Assumptions

To model the flow dynamics, we consider a two-layer porous medium with a permeability jump inclined at an angle θ to the horizontal (see figure 1.3). The upper and lower layer permeabilities and porosities are, respectively, (k_1, ϕ_1) and $(k_2 \ll k_1, \phi_2 = \phi_1 = \phi)$. The two-dimensional co-ordinate system is represented by (X, Z). The up- and downdip gravity currents are fed by a plume whose source is located a vertical height $Z = H$ above the permeability jump at the point where $X = 0$.

The theoretical model is based on several underlying assumptions. In addition, the lower layer is considered infinitely deep while the upper layer is, in most of the analysis to follow, assumed finite in vertical extent. Although the source fluid has a density, ρ_s, that is moderately larger than the density, ρ_0, of the ambient fluid, we assume that the viscosity contrast is small. Likewise, we ignore capillary effects and so perform our analysis is performed in the large Bond number limit and without reference to the possibility of residual trapping. We also ignore spatial variations of the density within the up- and downdip gravity currents assuming these to be small by comparison to the density contrast between the gravity current and the ambient. The gravity currents are assumed to be long and thin such that a hydrostatic (sharp in-

terface) analysis of the type described by Huppert and Woods (1995) applies. Finally, and as regards the descending (and entraining) plume, we assume, consistent with Sahu and Flynn (2015), a moderate Péclet number, here defined as $\mathrm{Pe} = \frac{d_0 U_\tau}{D_d}$ where D_d is the molecular diffusion coefficient, d_0 is the mean grain diameter and U_τ is the average transport velocity. As a result of this last assumption, plume entrainment, which results in an increase of plume volume flux, q_p, with depth, is set less by diffusion and more by dispersion. The plume source volume flux per unit width is denoted as q_s. Correspondingly, the source buoyancy flux per unit width is given by $F_s = q_s g'_s$ where the reduced gravity is defined by $g'_s = g(\rho_s - \rho_0)/\rho_0 \ll g$.

The evolution of the up- and downdip gravity currents is given by a balance between inflow from the plume and outflow resulting from convective dissolution along the upper surface and draining along the lower surface. As we explain in subsection 2.4, and due to the slow but steady increase of the gravity current thickness (e.g. at $X = 0$), the volume flux supplied to the gravity current by the plume very gradually decreases. (By similar reasoning, the density of the fluid supplied to the gravity current very gradually increases.) The combined volumetric inflow (per unit width) to the up- and downdip gravity currents is $q_p(h_0)$ and the corresponding density is $\rho_p(h_0)$ where h_0 is the time-variable height of the gravity current at $X = 0$. Compared to a real flow where internal stratification is possible, at least theoretically, the spatially uniform density approximation is made for simplifying the computational model and supposes that the vertical distance of the nozzle from the permeability jump is not large. Accordingly, the density contrast between the up- and downdip gravity currents and the surrounding ambient is given by $\Delta\overline{\rho_c} = \overline{\rho_c} - \rho_o$, where $\overline{\rho_c} = \rho_p(h_0)$ is the gravity current density. The associated reduced gravity is then defined as $\overline{g'_c} = g(\Delta\overline{\rho_c}/\rho_o)$.

The dissolution of gravity current fluid into resident ambient fluid yields con-

23

taminated fluid that rises towards the source. As noted earlier, basal draining is the other route by which fluid discharged by the plume may exit the up- or downdip gravity current. In modeling this draining, we assume, consistent with Bharath et al. (2020), the across-jump pressure variation is approximately hydrostatic such that the (vertical) draining velocity is determined from the local gravity current height, h. Furthermore, and consistent with our treatment of dynamics in the upper layer, a sharp interface assumption is supposed to apply in the lower layer. By this assumption, $\overline{\rho_d} = \overline{\rho_c}$ in which $\overline{\rho_d}$ is the (spatially-averaged) density of the so-called draining fluid.

3.2 Gravity Currents

To model the macroscopic evolution of each of the up- and downdip gravity currents, a sharp interface model is utilized that takes into account the combined effects of advection, draining to the lower layer and dissolution to the upper layer. Dissolution is dynamically significant only along the upper interface because its onset is controlled by forced or buoyancy driven flow at the early stages of injection (Huppert and Neufeld 2014). Although dissolution may likewise occur along the lower interface, this effect is immaterial to the dynamics of interest because of the speed at which discharged plume fluid falls through the lower layer.

Following the derivation presented in Bharath et al. (2020), the flow within the gravity current is assumed to obey Darcy's law and is treated as incompressible. Accordingly, the Darcy velocity of the gravity current is written as $\boldsymbol{u}_c \equiv (u_c, w_c)$ where u_c and w_c denote the along- and across-jump velocity components, respectively. For a permeability jump inclined at an angle θ to the horizontal, the hydrostatic pressure variation[1] in the across-jump direction

---

[1]We assume throughout our discussion that the Dupuit approximation applies such that the gravity current is long and thin such that pressure variations are indeed hydrostatic. We defer to a future study an exhaustive characterization of the range of p values for which

is given by

$$P_c(x, z, t) = p_c(x, t) - \overline{\rho_c} g z \cos \theta \tag{3.1}$$

where $p_c(x, t)$ is defined as

$$p_c(x, t) = P_o + (\overline{\rho_c} - \Delta \overline{\rho_c}) g x \sin \theta + \Delta \overline{\rho_c} g h \cos \theta \tag{3.2}$$

Here, P_0 is the pressure measured along the permeability jump at the origin and g is gravitational acceleration. Darcy's law yields expressions for the flow velocities in the along jump direction, i.e.

$$u_c = -\frac{k_1 \Delta \bar{\rho}_c g}{\mu} \begin{cases} \dfrac{\partial h}{\partial x} \cos \theta + \sin \theta, & [\text{Updip}, -x_{N_u} < x < 0] \\[3mm] \dfrac{\partial h}{\partial x} \cos \theta - \sin \theta, & [\text{Downdip}, 0 < x < x_{N_d}] \end{cases} \tag{3.3}$$

Here, μ is the dynamic viscosity. Additionally x_{N_u} and x_{N_d} respectively represent the gravity current nose positions in the up- and downdip directions. The spatio-temporal evolution equation for the gravity current thickness, h, is then obtained by substituting (3.3) into the depth-averaged continuity equation, which considers dissolution along the upper surface and basal draining along the lower surface. After some straightforward algebra, it can be shown that

$$\phi \frac{\partial h}{\partial t} = \begin{cases} \dfrac{k_1 \bar{g}'_c}{\nu} \dfrac{\partial}{\partial x} \left(h \dfrac{\partial h}{\partial x} \cos \theta + h \sin \theta \right) + w_{\text{drain}} - q_d, & [\text{Updip}, -x_{N_u} < x < 0] \\[4mm] \dfrac{k_1 \bar{g}'_c}{\nu} \dfrac{\partial}{\partial x} \left(h \dfrac{\partial h}{\partial x} \cos \theta - h \sin \theta \right) + w_{\text{drain}} - q_d, & [\text{Downdip}, 0 < x < x_{N_d}] \end{cases} \tag{3.4}$$

where ν is the kinematic viscosity. Also $q_d \, (> 0)$ specifies the rate of convective dissolution and has units $(\text{m}^3/\text{s})/\text{m}^2$ where the denominator corresponds to the area of the upper surface. (We will define the convective dissolution rate more precisely in section 3.6). Meanwhile, $w_{\text{drain}} \, (< 0)$ is the draining velocity whose functional form is prescribed in the following subsection.

---

the Dupuit approximation can be formally justified. Suffice it to say here that a slender aspect ratio benefits from p values that are comparatively large.

3.3 Basal Draining

We now examine the dynamics associated with the draining of gravity current fluid into the lower layer whose depth we assume to be very large. We utilize Darcy's equation and define a Darcy velocity, $\boldsymbol{u}_d \equiv (u_d, w_d)$ where u_d and w_d respectively point along- and across-dip. Here, u_d is the along slope component of the Darcy velocity while w_d is the velocity component in the across-jump direction. In the special case of a horizontal permeability jump, u_d depend upon $\partial h/\partial x$ while w_d depends on h (Acton et al. 2001). More generally, the across-jump velocity is defined by equation 3.5 (Bharath et al. 2020)

$$w_d = -\frac{k_2 \Delta \overline{\rho_d} g}{\mu} \left(1 + \frac{h}{l'}\right) \cos \theta \qquad (3.5)$$

Here, $l' = l \cos \theta$ is the perpendicular distance between the permeability jump and the (bottom) edge of the draining fluid – see figure 1.3. When $\theta \neq 0°$, $|u_d| \approx |w_d| \tan \theta$, and thus we can disregard u_d for small and moderate jump angles. If the thickness of draining fluid is significantly larger than the gravity current thickness such that $l' > h$, w_{drain} remains oriented in the vertical direction.

Combining the expression for draining velocity with an expression of mass balance for the fluid draining into the lower layer, we get

$$\phi \frac{\partial l}{\partial t} = -w_{\text{drain}} = -\sqrt{u_d^2 + w_d^2} = \frac{k_2 \Delta \overline{\rho_d} g}{\mu} \left(1 + \frac{h}{l} \cos \theta\right), \quad [-x_{N_u} < x < x_{N_d}]$$

$$(3.6)$$

where w_{drain} is the vertical draining velocity defined in figure 1.3. Unlike Bharath et al. (2020), we do not suppose any mixing between the draining and ambient fluids and thus $\rho_0 = \overline{\rho_d}$.

3.4 Gravity current source

Because of the gradual thickening of the gravity currents, the plume entrains ambient fluid over a vertical distance that slowly decreases in time. The plume volume flux per unit width at the upper surfaces of the up- and downdip gravity currents is given by (2.24) of Sahu and Flynn (2015), i.e.

$$q_p = \left[\left(\frac{16 F_s k_1}{\pi \nu} \right)^2 \phi \alpha (H + Z_s - h_0 \cos \theta) \right]^{\frac{1}{4}} \tag{3.7}$$

Here α is the transverse dispersivity, which depends on the mean grain diameter (Delgado 2007). Analogous to (3.7), and consistent with (2.25) of Sahu and Flynn (2015), we write

$$g_c' = \left[\left(\frac{\pi F_s \nu}{16 k_1} \right)^2 \frac{1}{\phi \alpha (H + Z_s - h_0 \cos \theta)} \right]^{\frac{1}{4}} \tag{3.8}$$

where $Z_s = \dfrac{1}{\phi \alpha} \left(\dfrac{\pi \nu}{16 F_s k_1} \right)^2 q_s^4$ is defined as the finite source correction term and is calculated with reference to the source volume flux per unit width, q_s, and the source buoyancy flux per unit width, F_s. Applying (3.7) and (3.8), (3.4) and (3.6) can be respectively re-written as

$$\frac{\partial h}{\partial t} = \begin{cases} \beta (1 - \chi h_{0^-} \cos \theta)^{-\frac{1}{4}} \left[\dfrac{\partial}{\partial x} \left(h \dfrac{\partial h}{\partial x} \cos \theta + h \sin \theta \right) - K \left(1 + \dfrac{h}{l} \cos \theta \right) \right] - \dfrac{q_d}{\phi}, \\ \qquad\qquad\qquad\qquad\qquad\qquad\qquad\qquad [\text{Updip}, -x_{N_u} < x < 0] \\ \beta (1 - \chi h_{0^+} \cos \theta)^{-\frac{1}{4}} \left[\dfrac{\partial}{\partial x} \left(h \dfrac{\partial h}{\partial x} \cos \theta - h \sin \theta \right) - K \left(1 + \dfrac{h}{l} \cos \theta \right) \right] - \dfrac{q_d}{\phi}, \\ \qquad\qquad\qquad\qquad\qquad\qquad\qquad\qquad [\text{Downdip}, 0 < x < x_{N_d}] \end{cases} \tag{3.9}$$

and

$$\frac{\partial l}{\partial t} = \beta K \begin{cases} (1 - \chi h_{0^-} \cos \theta)^{-\frac{1}{4}} \left(1 + \dfrac{h}{l} \cos \theta \right), & [\text{Updip}, -x_{N_u} < x < 0] \\ \\ (1 - \chi h_{0^+} \cos \theta)^{-\frac{1}{4}} \left(1 + \dfrac{h}{l} \cos \theta \right), & [\text{Downdip}, 0 < x < x_{N_d}] \end{cases} \tag{3.10}$$

27

where $K = k_2/k_1$ is the ratio of lower- to upper-layer permeability, and β is a velocity parameter defined as

$$\beta = \frac{k_1}{\phi\nu}\left[\left(\frac{\pi F_s\nu}{16k_1}\right)^2 \frac{1}{\phi\alpha(H+Z_s)}\right]^{\frac{1}{4}} \tag{3.11}$$

3.5 Initial and Boundary Conditions

At $t = 0$, the porous medium is fully saturated with ambient fluid such that $h = l = 0$. For $t > 0$, (3.9) and (3.10) require specification of an influx boundary condition such that the combined time rate of volume increase of the up- and downdip gravity currents matches q_p as specified by (3.7). For the simple case of a horizontal permeability jump with $\theta = 0°$, discharged plume fluid is divided equally between the up- and downdip directions. For $\theta > 0°$, we denote the dimensionless volume fraction of the flow propagating downdip as f_a. The influx boundary conditions then read as follows (Bharath et al. 2020):

$$\beta^2\left(h\frac{\partial h}{\partial x}\cos\theta + h\sin\theta\right)\Big|_{0^-} = -(1 - f_a)\Gamma(1 - \chi h_{0^-}\cos\theta)^{\frac{1}{2}}$$

$$\tag{3.12}$$

$$\beta^2\left(h\frac{\partial h}{\partial x}\cos\theta - h\sin\theta\right)\Big|_{0^+} = -f_a\Gamma(1 - \chi h_{0^+}\cos\theta)^{\frac{1}{2}}$$

Here $\Gamma = (k_1 F_s)/(\phi^2\nu)$ is defined as the buoyancy flux factor. The left hand side terms signify the time rate of increase of gravity current volume while the terms on the right hand side denote the volume of fluid discharged by the plume along the up- and downdip directions. In solving the governing equations (3.9) and (3.10), (3.12) is applied in conjunction with the following

condition of height continuity:

$$h_{0-} = h_{0+} \tag{3.13}$$

This last result allows us to solve for f_a at each time step. Meanwhile, the noses of the gravity currents in the up- and downdip directions are subject to the boundary conditions

$$h_{-x_{N_u}} = l_{-x_{N_u}} = 0 \qquad \text{and} \qquad h_{x_{N_d}} = l_{x_{N_d}} = 0 \tag{3.14}$$

3.6 Non-dimensionalization

Similar to Goda and Sato (2011), we define the following space and time scales to non-dimensionalise the governing equations:

$$\Pi_x = \frac{q_p|_{h=0}}{\phi\beta} \qquad \text{and} \qquad \Pi_t = \frac{q_p|_{h=0}}{(1 - \delta\cos\theta)^{-\frac{1}{4}}\phi\beta^2} \tag{3.15}$$

Here,

$$\delta = \frac{16}{\pi}\left(\frac{\phi\alpha}{H + Z_s}\right)^{\frac{1}{2}} \tag{3.16}$$

Thus do we define non-dimensional (starred) parameters, i.e.

$$x^* = \frac{x}{\Pi_x}, \qquad h^* = \frac{h}{\Pi_x}, \qquad l^* = \frac{l}{\Pi_x}, \qquad t^* = \frac{t}{\Pi_t} \tag{3.17}$$

Accordingly, (3.4) and (3.6) can respectively be rewritten as

$$\frac{\partial h^*}{\partial t^*} = \begin{cases} \left(\dfrac{1 - \delta h_{0-}^* \cos\theta}{1 - \delta\cos\theta}\right)^{-\frac{1}{4}} \left[\dfrac{\partial}{\partial x^*}\left(h^*\dfrac{\partial h^*}{\partial x^*}\cos\theta + h^*\sin\theta\right) - K\left(1 + \dfrac{h^*}{l^*}\cos\theta\right)\right] - Q_d, \\ \qquad\qquad\qquad\qquad\qquad\qquad\qquad\qquad [\text{Updip, } -x_{N_u}^* < x^* < 0] \\ \left(\dfrac{1 - \delta h_{0+}^* \cos\theta}{1 - \delta\cos\theta}\right)^{-\frac{1}{4}} \left[\dfrac{\partial}{\partial x^*}\left(h^*\dfrac{\partial h^*}{\partial x^*}\cos\theta - h^*\sin\theta\right) - K\left(1 + \dfrac{h^*}{l^*}\cos\theta\right)\right] - Q_d, \\ \qquad\qquad\qquad\qquad\qquad\qquad\qquad\qquad [\text{Downdip, } 0 < x^* < x_{N_d}^*] \end{cases} \tag{3.18}$$

29

and

$$
\frac{\partial l^*}{\partial t^*} = K
\begin{cases}
\left(\dfrac{1 - \delta h_{0-}^* \cos\theta}{1 - \delta \cos\theta}\right)^{-\frac{1}{4}} \left(1 + \dfrac{h^*}{l^*}\cos\theta\right), & [\text{Updip},\ -x_{N_u}^* < x^* < 0] \\[3ex]
\left(\dfrac{1 - \delta h_{0+}^* \cos\theta}{1 - \delta \cos\theta}\right)^{-\frac{1}{4}} \left(1 + \dfrac{h^*}{l^*}\cos\theta\right), & [\text{Downdip},\ 0 < x^* < x_{N_d}^*]
\end{cases}
\tag{3.19}
$$

Here, Q_d specifies the non-dimensional convective dissolution rate. For the purposes of this study and with reference to figure 1, Q_d is assumed to take the following functional form (Szulczewski et al. 2013):

$$
Q_d = 10^{-p}
\begin{cases}
0, & 0 < t^* < t_0^* \\[2ex]
1, & t_0^* \leq t^* < t_0^* + t_1^* \\[2ex]
e^{-(t^* - t_1^* - t_0^*)/t_2^*}, & t^* \geq t_0^* + t_1^*
\end{cases}
\tag{3.20}
$$

in which p modulates the strength of the convective dissolution. In the context of real geological flows, p depends on reservoir conditions such as temperature, pressure and saline concentration in the groundwater (MacMinn et al. 2011; Zhang and Xu 2003). During the early diffusion phase (Bolster 2014), a finite amount of onset time is incurred for the convective instabilities to arise which is negligible compared to typical migration time scales (MacMinn et al. 2011). Consistent with MacMinn et al. (2011), we have considered a constant dissolution rate after the onset period which lasts until $t^* = t_0^* + t_1^*$. Once the buoyant fingers reach the ultimate extent of the finite upper layer, a curtain of contaminated fluid begins to sink down which then causes the rate of dissolution to decay in an exponential fashion (Szulczewski et al. 2013). The mode of decay is similar to the one explored in figure 5 on Hewitt et al. (2013). Equation 3.20 does not consider any flux loss from the gravity current due to residual trapping as witnessed in figure 1.1. Additionally, the complicated

dynamics of the fingering instabilities are simplified with macroscopic values of the dissolution rate in eq. (3.20).

At $t^* = 0$, the initial condition is $h^* = l^* = 0$. The dimensionless influx boundary conditions are

$$\left(h^* \frac{\partial h^*}{\partial x^*} \cos \theta + h^* \sin \theta \right) \bigg|_{0^-} = -(1 - f_a)(1 - \delta h^*_{0^-} \cos \theta)^{\frac{1}{2}}$$

$$\text{(3.21)}$$

$$\left(h^* \frac{\partial h^*}{\partial x^*} \cos \theta - h^* \sin \theta \right) \bigg|_{0^+} = -f_a(1 - \delta h^*_{0^+} \cos \theta)^{\frac{1}{2}}$$

By utilizing Π_x and Π_t, the factor Γ that appears in (3.12) gets cancelled out and is thus absent in the dimensionless equations. Equations (3.21) are applied subject to

$$h^*_{0^-} = h^*_{0^+} \qquad \qquad \text{(3.22)}$$

Finally, and at the gravity current fronts, we require that

$$h^*_{-x^*_{Nu}} = l^*_{-x^*_{Nu}} = 0 \qquad \text{and} \qquad h^*_{x^*_{Nd}} = l^*_{x^*_{Nd}} = 0 \qquad \text{(3.23)}$$

Chapter 4

Model Results

4.1 Constant Dissolution Rate

The principal focus of this study is cases where the dissolution rate decreases with time in the manner suggested by figure 1.2. However, and for comparison's sake, it is helpful to generate a series of "baseline" solutions having a constant dissolution rate. In the context of figure 1.2, we therefore consider the limit $t_1^* \to \infty$. Analogously, and consistent with the medium geometry studied by Goda and Sato (2011) and Bharath et al. (2020), we suppose that the upper layer depth is very large. We solve the dimensionless governing equations (3.18) and (3.19) numerically using a forward finite difference scheme with a grid size $\Delta x^* = 6 \times 10^{-2}$ and a time step $\Delta t^* = 9 \times 10^{-4}$. The source volume flux is assumed constant suggesting a continual (if very moderately decreasing) supply of fluid to the up- and downdip gravity currents.

Figure 4.1 considers the effect of the exponent p from (3.20). The figure exhibits snapshot images showing the temporal evolution for a case where $\theta = 20°$. For such a large value of θ, there exists a pronounced asymmetry between the up- and downdip flows. So although h^* varies linearly with x^* for $x^* < 0$ and $x^* > 0$ (Pritchard 2007; Goda and Sato 2011), there is a significant difference of run-out length up- vs. downdip. When $p = \infty$, the dissolution strength is vanishingly small and thus the gravity currents travel
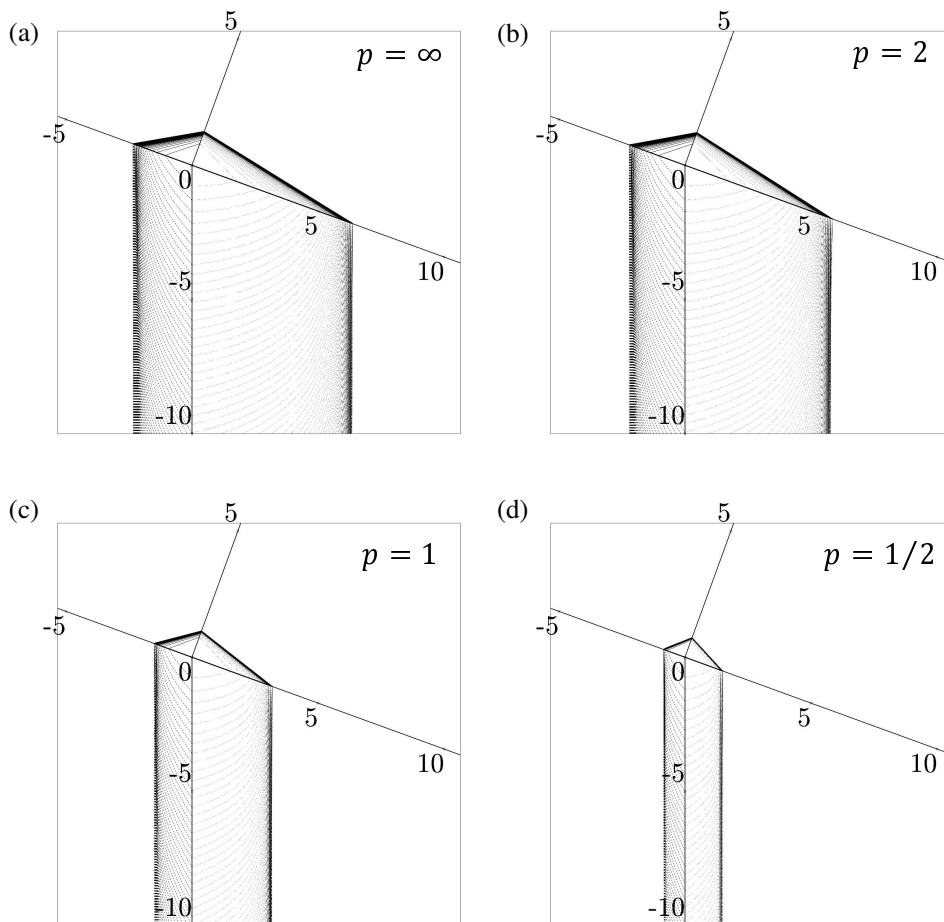
Figure 4.1: Spatial-temporal evolution of the gravity currents and draining flow for an inclined permeability jump characterized by a jump angle of $\theta = 20°$. The time increment between gravity current profiles measures the gravity current height, h^* and draining layer depth, l^*. Panels a, b, c and d respectively consider $p = \infty$, $p = 2$, $p = 1$ and $p = 1/2$.
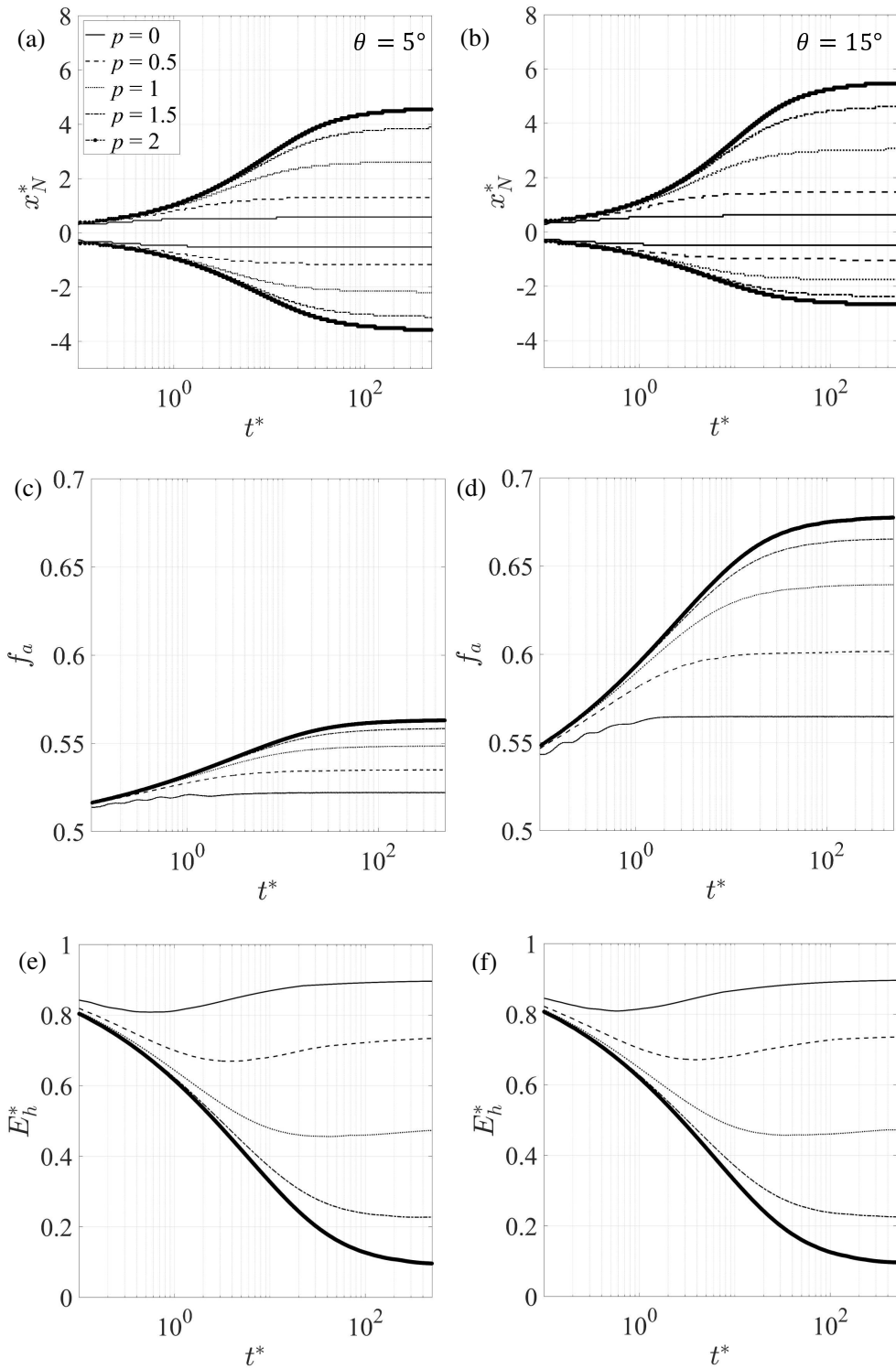
Figure 4.2: Gravity current nose position vs. time for (a) $\theta = 5°$ and (b) $\theta = 15°$. Downdip volume fraction vs. time for (c) $\theta = 5°$ and (d) $\theta = 15°$. Storage efficiency vs. time for (e) $\theta = 5°$ and (f) $\theta = 15°$.

34

the greatest distances. Increasing the dissolution strength by decreasing p reduces the run-out lengths in a monotone fashion.

The significance of p is further explored in figure 4.2. Figures 4.2 a,b depict for $\theta = 5°$ and $\theta = 15°$, respectively, the time evolution of the nose positions, x_N^*, of the up- and downdip gravity currents. In both panels, a range of values for p are considered. Not unexpectedly, a greater up- vs. downdip flow asymmetry is seen for the larger value of θ. Also, and consistent with figure 4.1, the gravity currents travel greater distances along the permeability jump as p is increased and the relative importance of dissolution is curtailed. Stated differently, increasing the dissolution strength facilitates rapid mixing of discharged plume fluid with the overlying ambient leading to shorter run-out lengths. Solutions exhibit the greatest sensitivity to p on the downdip side for relatively large permeability jump angles. By contrast, dissolution has a weaker influence on the updip side where gravity is often as or more important in arresting the gravity current flow. Considering the same range of p as in figures 4.2 a,b, figures 4.2 c,d show for $\theta = 5°$ and $\theta = 15°$, respectively, the time evolution of f_a. In both panels, f_a increases sharply at first and then later plateaus as the up- and downdip flows approach their respective run-out lengths.

To gauge the effectiveness of dissolution as a long-term storage mechanism in an unconfined layer of infinite depth, reference is drawn to the storage efficiency, E_h^*. Consistent with MacMinn et al. (2011) and at any particular instant in time, we define the storage efficiency as the ratio of the discharged plume fluid volume retained in the upper layer to the cumulative volume of plume fluid discharged by the source. So defined, the storage efficiency is a key parameter in assessing the storage capacity of e.g. aquifers: the larger E_h^*, the greater the volume of injectate that can be securely sequestered. In symbols,

E_h^* is expressed as follows:

$$E_h^* = \frac{V_{\text{retained}}(t)}{V_{\text{injected}}(t) + V_{\text{entrained}}(t)} \qquad (4.1)$$

Here V_{retained} is the net volume of discharged plume fluid retained in the upper layer as a result of dissolution and up- and downdip advection. Meanwhile, $V_{\text{injected}} = \int_0^t Q_{\text{source}} \, dt$ in which Q_{source} is the plume source volume flux. Finally, $V_{\text{entrained}}$ is the volume of upper layer ambient fluid entrained into the descending plume. Because $V_{\text{retained}} = V_{\text{injected}} + V_{\text{entrained}} - V_{\text{drained}}$, it can be shown that

$$E_h^* = 1 - \frac{V_{\text{drained}}(t)}{V_{\text{injected}}(t) + V_{\text{entrained}}(t)} \qquad (4.2)$$

Given the sharp interface approximation applied to the draining flow, the numerator of the latter right-hand side term is straightforward to calculate as compared to the numerator of (4.1). Figures 4.2 e,f show for $\theta = 5°$ and $\theta = 15°$, respectively, the variation of E_h^* with time for different dissolution strengths. For small p, the storage efficiency displays a decrease at early times after which it rebounds then plateaus in the long time limit. The shape of the curves is explained as follows: at early times, the thickness of the gravity currents remain modest as a result of which there is comparatively little draining into the lower layer. Over time, the gravity current thickness increases, drainage into the lower layer becomes more robust and consequently E_h^* falls. Simultaneously, however, the gravity current elongates thereby providing more surface area along which dissolution can take place. This causes dissolution to dominate over draining as a result of which the storage efficiency increases for sufficiently large t^*. In essence, thickness is punished by draining (which decreases E_h^*) whereas large lateral extents are punished by dissolution (which increases E_h^*). When p is large, by contrast, dissolution remains subordinate to draining even when the gravity currents have extended to long lengths. As a consequence, and for $p \gtrsim 1.5$, E_h^* is a monotone decreasing function of time.
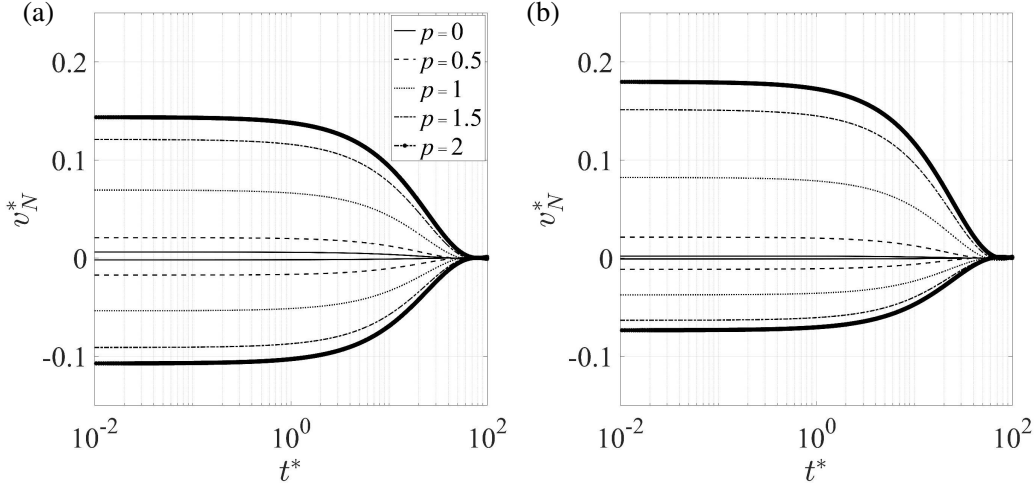
Figure 4.3: Gravity current spreading velocity, v_N^* vs. time for (a) $\theta = 5°$ and (b) $\theta = 15°$

Accordingly, we observe from figures 4.2 e,f an inverse relationship between E_h^* and p. As expected from (4.1), stronger dissolution leads to larger storage efficiencies both in the short and long term. Additionally, and in contrast to the panel pairs figure 4.2 a,b and 4.2 c,d, the storage efficiency is largely unaffected by the permeability jump angle: as θ increases, the downdip gravity current elongates but the updip gravity current shortens, i.e. the total surface area available for dissolution is comparable whether θ is large or small.

Utilizing data from figure 4.2 a,b, figure 4.3 a,b depicts the temporal evolution of the gravity current spreading velocity, $v_N^* = dx_N^*/dt^*$. Initially the dynamics of the gravity current are fast paced, owning to the small degree of drainage as a result of low thickness and likewise small dissolution because of the gravity current's small areal footprint. These losses from the gravity current fluid even when combined is dwarfed largely by the predominant advection rate, which leads to large initial velocities. Later on, as the gravity currents experiences further lateral extension due to high initial spreading velocities,

its elongated interface opens up further areas for dissolution to the ambient. As a consequence the amount dissolution quickly picks up. Notwithstanding the aforementioned phenomena, the draining to the lower layer becomes more pronounced and the combined increases in these system losses serves to rapidly deplete the gravity current's forward momentum. This is shown in the graph as a period of rapid deceleration during which time the high initial velocities decrease in a monotone fashion to zero at the point of terminal run-out. The rate of decrease of velocity falls over time since the deceleration rate is a direct function of fresh areas opening up for dissolution, which near the point of terminal run-out is trivial. From the figure we observe that convective dissolution limits the maximum nose velocity, both in the up- and downdip direction of the gravity current flow. Further, decreasing p which signifies an increase in the dissolution strength, reduces the nose velocity of the gravity current throughout until it comes to a complete stop. Comparing fig. 4.3 b with fig. 4.3 a, a higher tilt angle $\theta = 15°$ in the former, leads to large dissimilarities in the flow velocities. Because of gravity assist, during the early time dynamics the downdip flows are faster compared to the updip case. However the time taken for the gravity current to become stationary remains a strong function of the dissolution strength. A decrease in p results in the gravity current stopping more quickly.

Synthesizing data from figures like figures 4.2 a,b, figure 4.4 shows a surface plot of gravity current run-out lengths as a function of the dissolution strength, p, and the permeability jump angle, θ. Here θ in the range from $\theta = -20°$ to $\theta = 0°$ shows run-out lengths measured updip while θ in the range from $\theta = 20°$ to $\theta = 0°$ shows run-out lengths measured downdip. When $\theta = 0°$ and the permeability jump is horizontal, the run-out lengths in the up- and downdip directions are equal. Asymmetry is obviously introduced by considering $\theta \neq 0°$, however significant differences between the up- and downdip directions arise
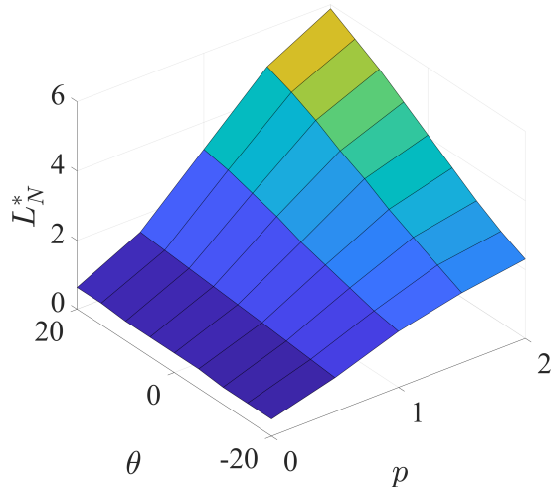
Figure 4.4: [Color online] Run-out lengths, up- and downdip as a function of the dissolution strength, p, and permeability jump angle, θ (measured in degrees).

only for sufficiently large p. In such cases, dissolution is comparatively weak and so differences between the up- and downdip flows are not masked by mass loss to the upper layer ambient. In the $p \to 0$ limit, by contrast, the dissolution rate is large, therefore the run-out lengths show a relative insensitivity to θ and the gravity currents travel relatively short distances along the permeability jump. In this regime of small p, dissolution dominates over advection such that gravity current motion along the permeability jump is hindered.

4.2 Convective Dissolution with Simultaneous Shutdown

In this subsection, we consider the case where t_1^* is finite and, after a time t_1^* the dissolution rate decreases in a spatially uniform way. Throughout this subsection, t_0^* is assumed to be 0. Figures 4.5 a,c compare the temporal evolution of the gravity current nose for $\theta = 5°$ and $\theta = 15°$, respectively. In both panels, we consider $t_2^* = 50$ and a range of values for t_1^*. When $t_1^* = 0$, we implicitly assume an upper layer that is thin so that the rate of dissolution

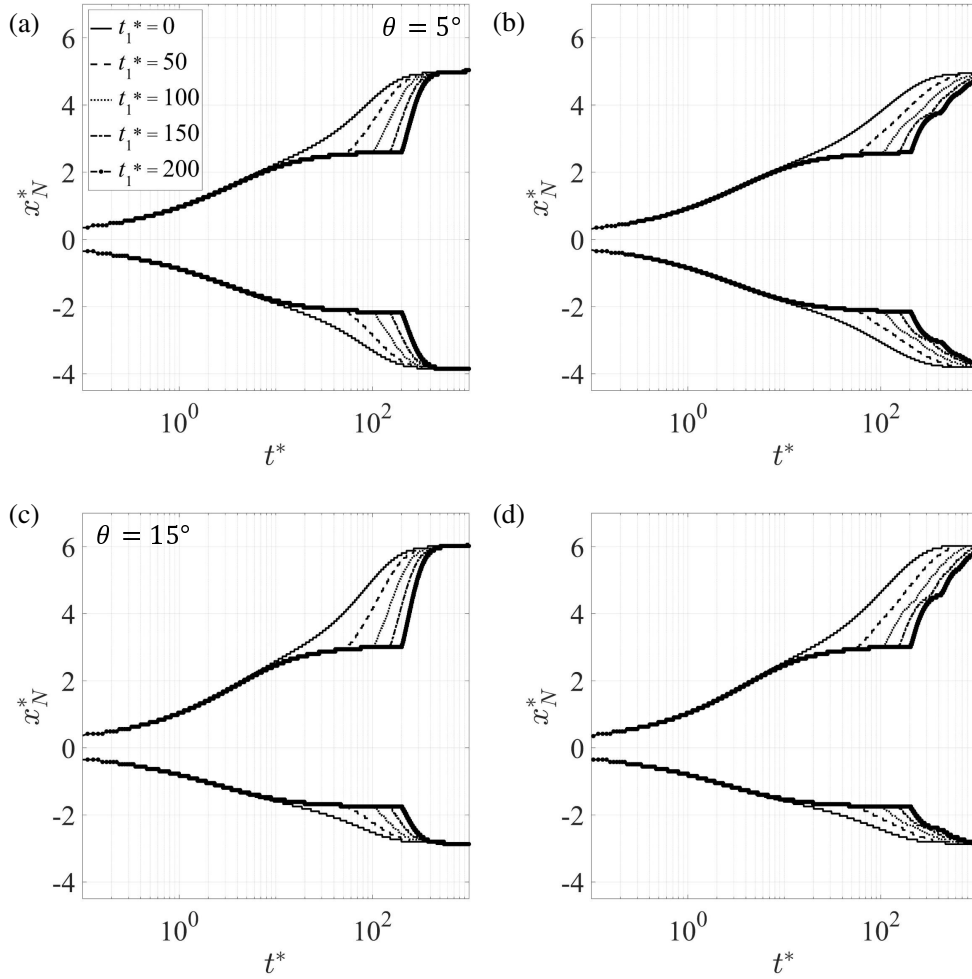Figure 4.5: Nose positions, both up- and downdip, for $p = 1$, $t_2^* = 50$ and various values of t_1^* (a, b) $\theta = 5°$, (c, d) $\theta = 15°$. The left- and right-hand side panels respectively consider simultaneous and sequential shutdown.

begins to slow immediately. Conversely, large t_1^* corresponds to an upper layer of sufficient depth that a constant rate of dissolution is realized for nontrivial time. Similar to the results of the previous subsection and considering the downdip flow, curves of x_N^* increase in a monotone fashion and later plateau provided t_1^* is not small. For $t^* > t_1^*$, the front is remobilized and there appears a second regime of gravity current advance. In the long-time limit, all of the curves in figure 4.5 a or in figure 4.5 c approach the same limiting value. This coincidence is expected because all of the cases considered share the same dissolution strength, $p = 1$, and permeability jump angle, θ. As such, the same volume of discharged plume fluid is ultimately dissolved into the upper layer, irrespective of the varying intermediate dynamics associated with different t_1^*. We refer to the plateaus experienced at moderate and late times as intermediate and terminal run-out, respectively. In the former case, the sum of the rates of draining and dissolution matches the rate at which fluid is supplied to the gravity current by the descending plume. Once $t^* > t_1^*$, some fraction of the fluid that would have dissolved into the upper layer instead accumulates in the gravity current. As a result, the gravity current height increases leading to front remobilization (and additional draining). Although the surface area available for dissolution increases as the gravity current elongates, dissolution decreases overall as required by figure 1. When, in the long-time limit, the gravity current stops for a second time, there is a balance between the rates of influx and mass loss due to draining.

To better characterize the flow asymmetries arising from the previous cases, we plot in figures 4.6 a,c, respectively, the time variation of f_a for $\theta = 5°$ and 15°. During re-mobilization, f_a increases more rapidly with time than for $t^* < t_1^*$. As terminal run-out is approached, f_a approaches a constant, the precise value of which depends, at least in part, on θ: as θ increases, so too does the downdip volume fraction.
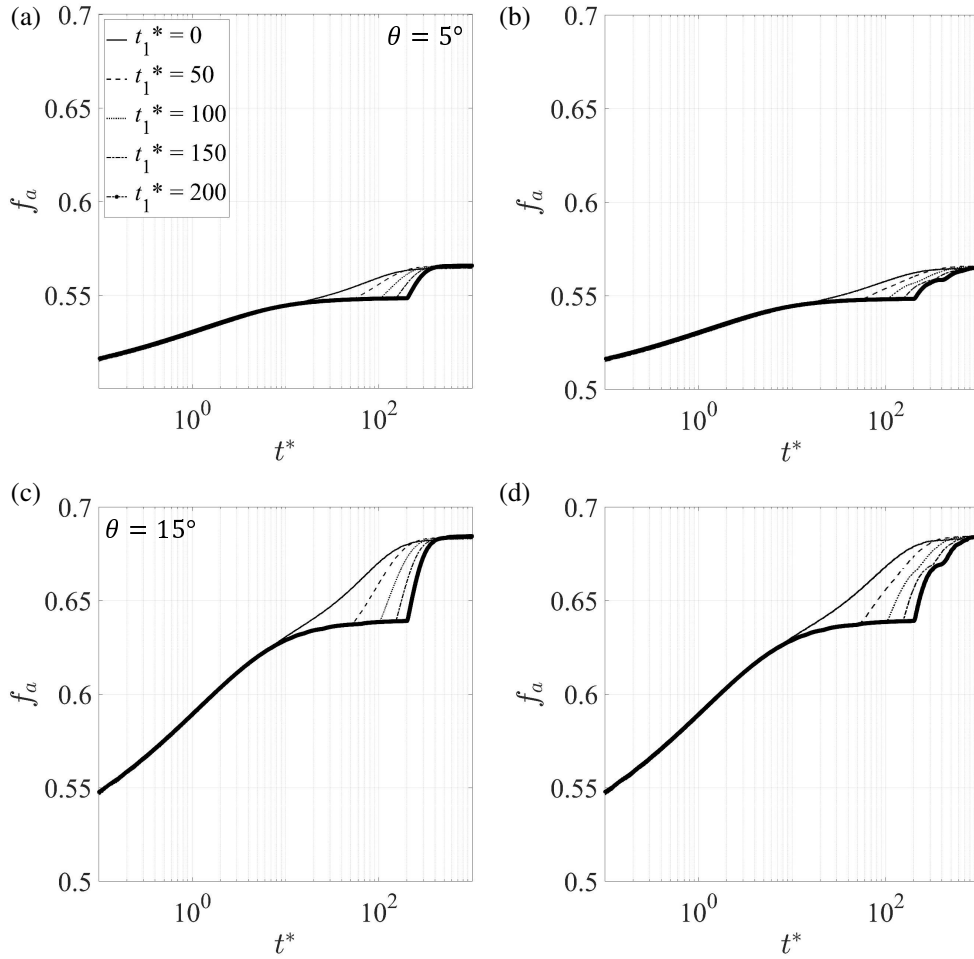
Figure 4.6: As in figure 4.5 but considering the downdip volume fraction, f_a.

Complementing figures 4.5 and 4.6, figure 4.7 shows the time variation of the storage efficiency. At early times when the rate of draining is relatively small, a sizeable fraction of the fluid discharged by the plume is retained in the upper layer. Relative to the semi-log axes used in figure 4.7, the storage efficiency experiences an almost linear decrease as the gravity current continues to spread. When $t_1^* > 0$, the storage efficiency gradually plateaus as the gravity current reaches intermediate run-out in which case there is a fixed balance between drainage and dissolution (not yet diminished). Once $t^* = t_1^*$, this balance is disrupted so as to favor draining; correspondingly, E_h^* again begins to fall. In the shutdown regime, larger values of t_1^* lead to larger values of the storage efficiency. Note, however, that whatever the (finite) value of t_1^* and, by extension, whatever the thickness of the upper layer, E_h^* must approach zero in the long time limit. Furthermore and consistent with figures 4.2 e,f, there is little variation of the storage efficiency with θ.

Figure 4.8 a illustrates, in the t_1^*-θ parameter space, a surface plot showing the non-dimensional time, t_{95}^*, to reach 95% of terminal run-out. Similar to figure 4.4, results are displayed for up- and downdip flow. For fixed θ, figure 4.8 a indicates that t_{95}^* increases with t_1^*: larger t_1^* delays the onset of shutdown and, by extension, extends the time spent in intermediate run-out.

Till now, our emphasis has been to characterize the influence of t_1^*, the time over which the dissolution rate is constant. We have therefore considered a fixed value for t_2^*, the e-folding decay time that characterizes the rate at which dissolution eventually diminishes. In the interests of presenting a balanced discussion, we shall now assume a fixed value for t_1^* and explore the influence of t_2^*. To this end, figure 4.9 shows the time variation of the up- and downdip nose positions for various t_2 and $\theta = 0°$ (panel a) and $\theta = 15°$ (panel c). We observe in figure 4.9 a that the nose advances rapidly at early times but then decelerates and very nearly stops by $t^* = t_1^* = 50$. For $t^* \geq 50$, the rate of convective
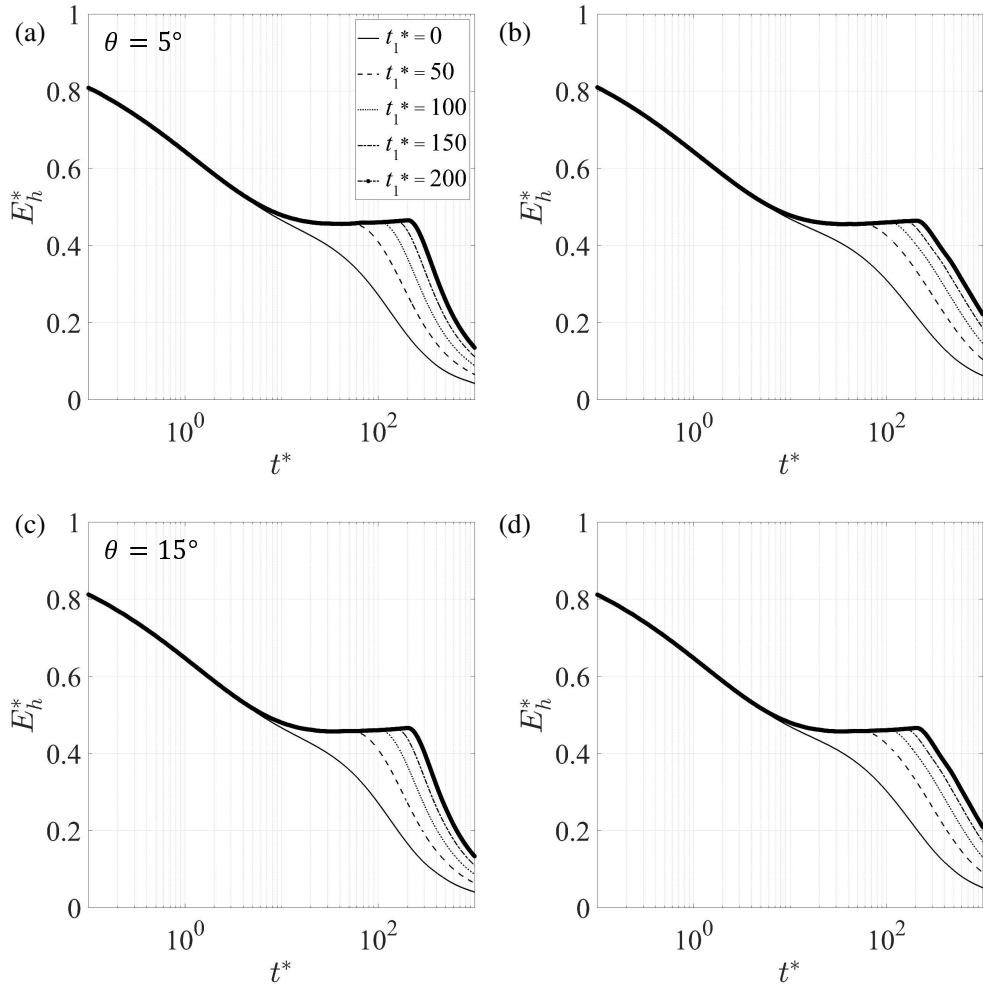
Figure 4.7: As in figure 4.5 but considering the storage efficiency, E_h^*
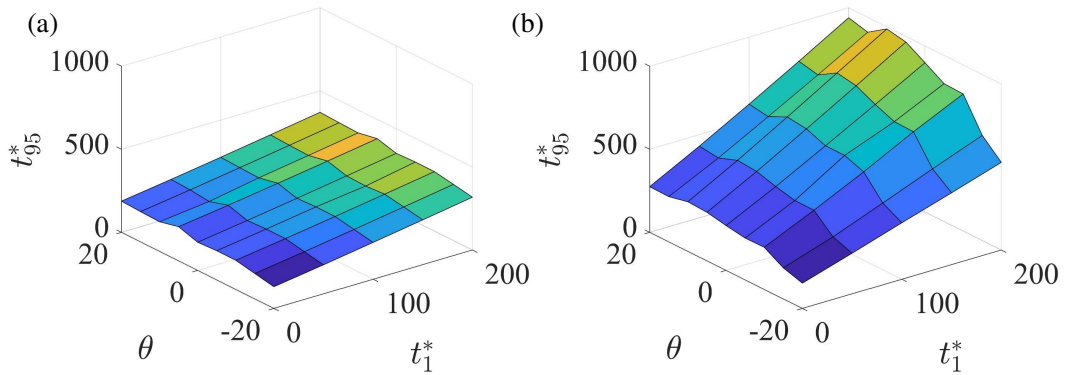
Figure 4.8: [Color online] Time, t_{95}^*, to reach 95% of terminal run-out vs. t_1^* and θ (measured in degrees) for (a) simultaneous shutdown and (b) sequential shutdown.
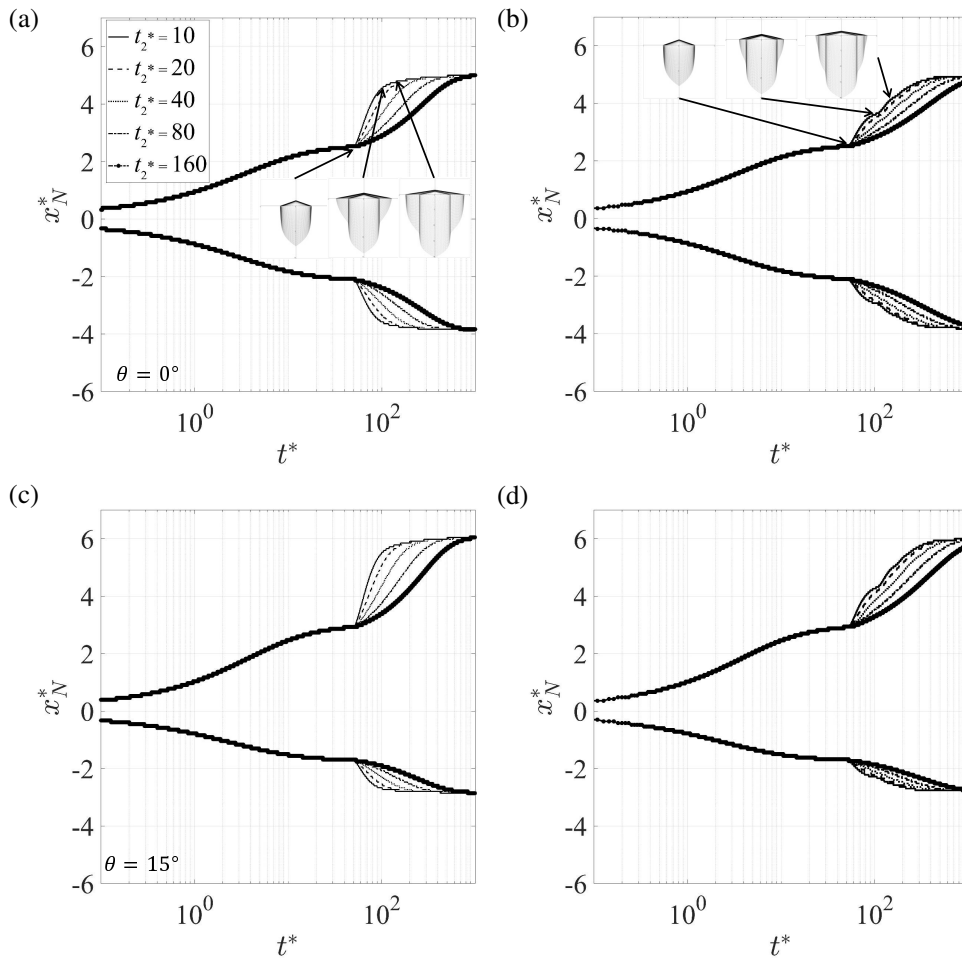
Figure 4.9: As in figure 4.5 but for various t_2^* and $t_1^* = 50$. The inset images in panels a and b provide snapshots of the discharged plume fluid at $t^* = 50, 100$ and 150.
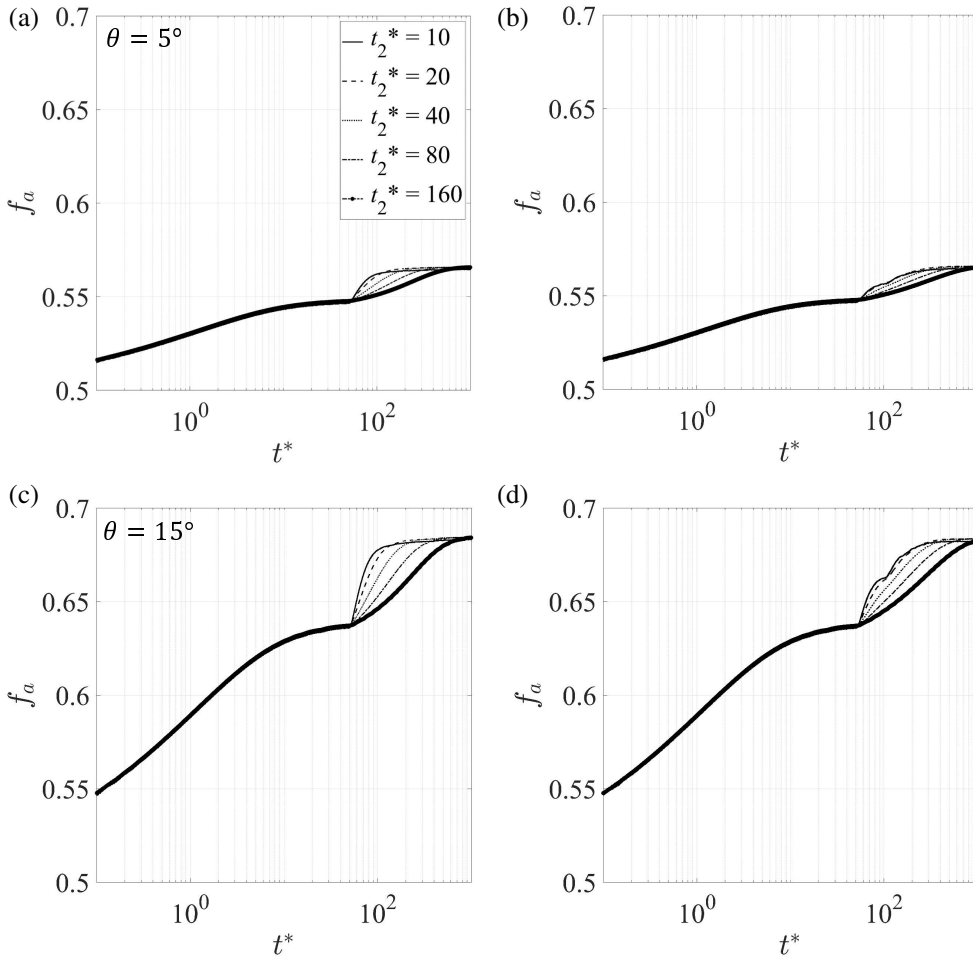
Figure 4.10: As in figure 4.6 but for various t_2^* and $t_1^* = 50$.

dissolution begins to decrease. When t_2^* is comparatively small, convective dissolution falls sharply leading to a more rapid remobilization of the gravity current. For larger t_2^*, convective dissolution arrests more slowly and the up- and downdip propagation of the gravity currents during remobilization is more leisurely. Figures 4.9 a,c confirm that the terminal run-out lengths, though dependent on θ, do not vary with t_2^*.

To characterize the extent of flow asymmetry before and during shutdown, fig. 4.10 shows the time variation of f_a as a function of t_2^* for $\theta = 5°$ (panel a) and $\theta = 15°$ (panel c). Figures 4.10 a,c exhibit similar behavior to that
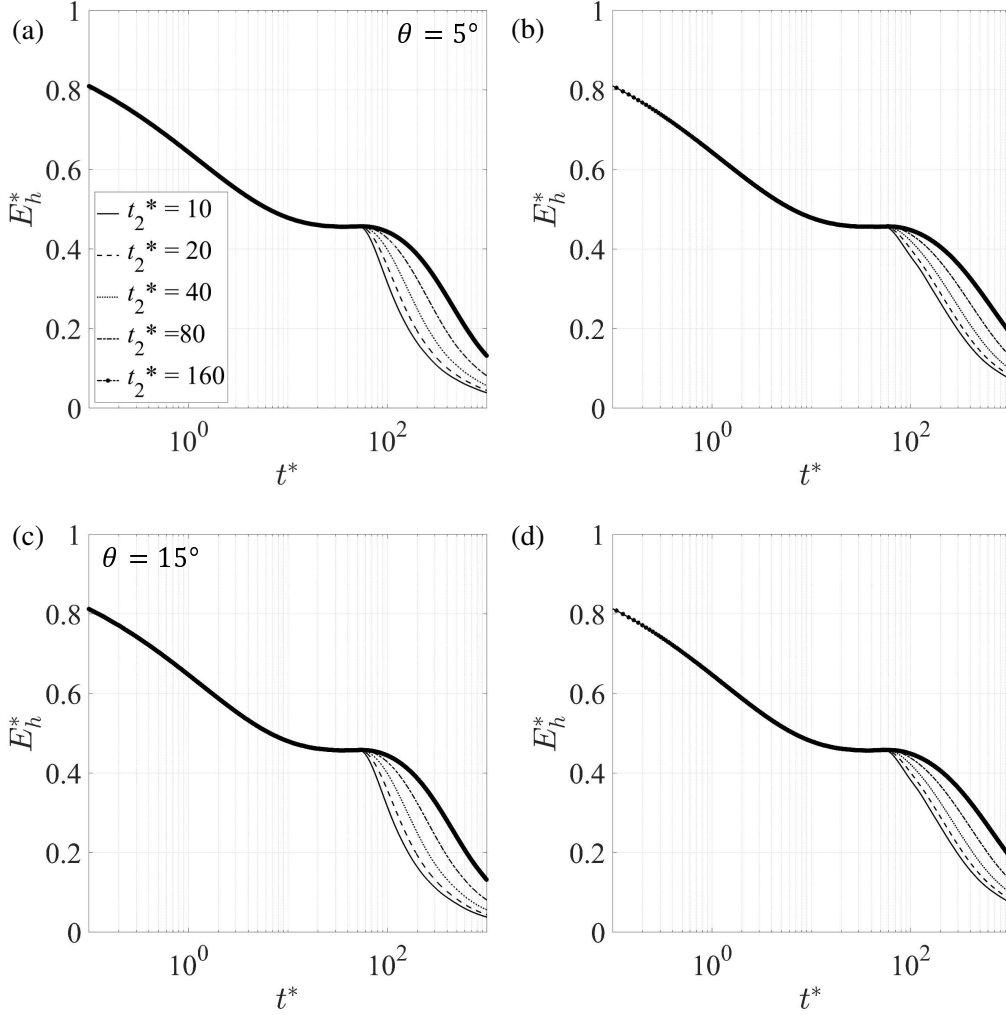
Figure 4.11: As in fig. 4.6 but for various t_2^* and $t_1^* = 50$.

observed in figures 4.6 a,c, i.e. f_a increases so long as the gravity currents are propagating but plateaus when the gravity currents become arrested, either temporarily or permanently. Not surprisingly then, and for $50 < t^* < \infty$, f_a is larger for smaller t_2^*.

Similar to figure 4.7, figure 4.11 shows the variation of the storage efficiency, E_h^*, with t_2^*. Because E_h^* characterizes the ability to store discharged plume fluid in the upper layer, the volume retained changes significantly with t_2 in the shutdown regime. When t_2^* is large, the rate of convective dissolution remains

47
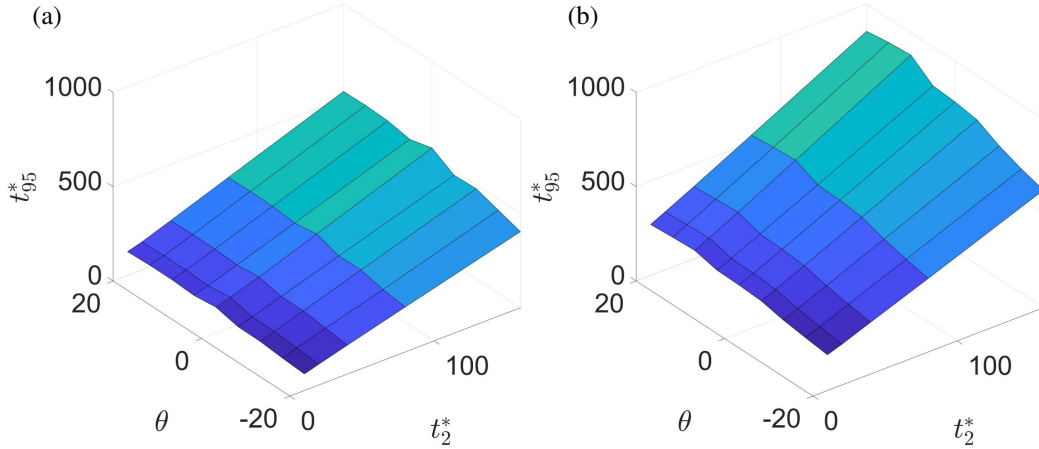
Figure 4.12: [Color online] As in figure 4.8 but with t_2^* rather than t_1^* $(= 50)$ as an independent variable.

elevated for comparatively long periods of time and hence E_h^* is likewise large. Also consistent with figure 4.7, we observe from figure 4.11 that $E_h^* \to 0$ in the long time limit, regardless of the value of t_2^*.

Figure 4.12 illustrates the time, t_{95}^*, taken to reach 95% of terminal run-out as a function of t_2^* and θ. When the latter variable is fixed, and consistent with figure 4.9, t_{95}^* increases with t_2^*. For prescribed t_2^*, there is a general, if modest, increasing trend of t_{95}^* with the permeability jump angle: as θ increases, the downdip gravity current travels comparatively long distances and so requires more time to reach terminal run-out.

4.3 Convective Dissolution with Sequential Shutdown

A defacto assumption of the previous subsection was one of very rapid horizontal mixing of the solute through the upper layer ambient such that the rate of dissolution was spatially uniform along the gravity current length. In this subsection, we examine the bookend opposite limit, i.e. one where the

rate of horizontal mixing is slow such that significant spatial variations of the dissolution rate may arise.

Similar to figures 4.5 a,c, figures 4.5 b,d show, for various t_1^*, the up- and downdip evolution of the gravity current nose but for the sequential shutdown case. In contrasting the panel pairs figure 4.5 a,b and c,d, similar behavior is observed with two notable exceptions. Firstly, and because the cessation of dissolution is now more gradual, gravity current remobilization is more measured, both up- and downdip. Thus the kinks in the curves of figures 4.5 b,d that arise when $t^* \simeq t_1^*$ ($t_1^* = 0$ excepted) are less sharp. Secondly, and because remobilization is associated with the generation of new interfacial area directly below virgin ambient fluid, additional convective dissolution will occur after intermediate run-out. In general, such dissolution after-the-fact is more modest than that which occurred initially, i.e. for $t^* \leq t_1^*$. On the other hand, if t_1^* is sufficiently large, dissolution after-the-fact may be enough to again arrest the up- and downdip gravity currents. In figure 4.5 b,d, this behavior is most evident when $t_1^* = 200$. Here, the curves in question show an intriguing "stop-start" pattern whereby the gravity current is remobilized multiple times over as new interfacial area is created, dissolution disrupts the dynamical balance between draining and advection, dissolution then slows and stops all in a repetitive cycle. The sequence just described is arrested only by the approach to terminal run-out. Not surprisingly, terminal run-out lengths are the same in figures 4.5 b,d and figures 4.5 a,c, respectively. However, because the overall dissolution rate declines more gradually in the former two figures, the time to reach this asymptotic state is correspondingly larger, particularly for large t_1^*.

Similar to figures 4.6 a,c, figures 4.6 b,d show, for various t_1^*, the time variation of the downdip volume fraction, f_a. Consistent with the comparison between the figure pairs 4.5 a,b and 4.5 c,d, we note from figure 4.6 that sequential shutdown is associated with a more gradual remobilization process,

remobilization being associated with a sudden increase in f_a when $t^* \simeq t_1^*$ ($t_1^* = 0$ excepted). Also, the stop-start signatures evident in figures 4.5 b,d reappear in figures 4.6 b,d: as expected, gravity current remobilization and arrest impact the fraction of discharged plume fluid flowing up- vs. downdip.

Similar to figures 4.7 a,c, figures 4.7 b,d show, for various t_1^*, the time variation of the storage efficiency, E_h^*. Here, the differences between the left- and right-hand side panels are not as dramatic as observed in figures 4.5 and 4.6. Most obviously, figure 4.7 does not exhibit any manifestations of the stop-start behavior that are so prominent for large t_1^* in figures 4.5 and 4.6. Following intermediate run-out, the process of sequentially remobilizing then arresting the gravity current involves, first and foremost, a trade-off between advection and dissolution. Because both processes retain contaminated fluid in the upper layer (as compared to draining, which transports contaminated fluid to the lower layer), the start-stop impact on E_h^* is subdued and the inflections that characterize the large-t_1^* curves of figures 4.5 and 4.6 for sufficiently large t^* are absent in figure 4.7. We observe that, for $t^* \simeq t_1^*$ and excepting $t_1^* = 0$, the storage efficiencies predicted in figures 4.7 b,d decline less dramatically than do their counterparts from figures 4.7 a,c. Stated differently, and over the range of times considered in figure 4.7, fluid retention in the upper layer is larger for sequential shutdown, which culminates in higher storage efficiencies. For instance, and for sequential shutdown, E_h^* for $t_1^* = 200$ is 61.5% higher than the corresponding E_h^* value for simultaneous shutdown.

Similar to figure 4.8 a, figure 4.8 b shows the time, t_{95}^*, required for the up- and downdip gravity currents to reach 95% of their terminal lengths. Consistent with our discussion of figures 4.5 b,d, the time to reach terminal run-out is extended in the case of sequential shutdown, characterized as it is, for large t_1^*, by intermediate stages of arrested movement of varying intensity. To this end, t_{95}^* values are much larger for $t_1^* = 200$ where multiple starts and stops

are encountered as opposed to the case $t_1 = 0$ where the advance of the gravity currents is more regular.

Focusing now on the impact of the dissolution decay rate, figures 4.9 b,d show, similar to figures 4.9 a,c, the up- and downdip evolution of the gravity current nose for fixed t_1^* but different t_2^*. Similar to figures 4.5 b,d, and 4.6 b,d, inflections arise also in figures 4.9 b,d, i.e. for sufficiently small t_2^*. In this low-t_2^* limit, dissolution terminates quickly, leading to a more abrupt remobilization of the up- and downdip gravity currents. In turn, new interfacial area is likewise created relatively quickly thereby allowing new opportunities for dissolution, which ultimately arrest the gravity currents for a second time. For fixed (small) t_2^*, the intensity of the resulting behavior depends on the permeability jump angle. For instance, this intensity is relatively weak when considering large values of θ and updip flows (figure 4.9 d). On the other hand, and regardless of the permeability jump angle, no stop-start behavior is observed when t_2 surpasses a critical value of approximately 20 in which case new interfacial area is created too slowly to cause the up- and downdip gravity currents to stop a second time. Comparing the two regimes of convective dissolution, remoblization takes place more gradually for sequential shutdown for the same value of t_2^*.

In figure 4.9 a and figure 4.9 b, snapshot images showing the gravity currents and draining fluid are plotted for $t_2^* = 10$ at $t^* = 50$, $t^* = 100$ and $t^* = 150$. When $t^* = 50 \, (= t_1^*)$, the snapshot images pertaining to the two regimes are identical. Such equivalence is lost, however, once $t^* > t_1^*$. When $t^* = 100$ or, more especially, $t^* = 150$, figures 4.8 a and figure 4.8 b confirm that the gravity currents travel greater along-jump distances in the case of simultaneous shutdown.

Similar to figures 4.10 a,c, figures 4.10 b,d show, for various t_2^*, the time variation of the downdip volume fraction, f_a. For $t^* > t_1^*$, the curves of fig-

ures 4.10 b,d have gentler slopes than do their counterparts in figures 4.10 a,c, respectively. Figure 4.10 thereby provides more evidence that sequential shut-down is associated with a more gradual remobilization process. Also, and as expected, signatures of the stop-start behavior described in conjunction with figure 4.8 reappear in figure 4.10, most prominently when t_2^* is small and θ is large.

Similar to figures 4.11 a,c, figures 4.11 b,d show, for various t_2^*, the time variation of the storage efficiency, E_h^*. As with figure 4.7, the differences between the left- and right-hand side panels are relatively minor with the curves of panels b and d exhibiting, for $t^* > t_1^*$, gentler slopes. Also consistent with figure 4.6, the permeability jump angle has only a very minor impact on the storage efficiency, i.e. there is little difference between figures 4.11 a and 4.11 b or between figures 4.11 b and 4.11 d. This observation is again attributed to the fact that the combined length of the up- and downdip gravity currents remains largely unchanged as the permeability jump angle is varied. Thus as θ is increased, the along-jump distance travelled updip decreases while the corresponding distance propagated downdip increases in approximately equal measure.

Similar to figure 4.12 a, figure 4.12 b shows the time, t_{95}^*, required for the up- and downdip gravity currents to reach 95% of their terminal lengths. In contrasting the surface plot of figure 4.12 b with that of figure 4.12 a, we find that for prescribed θ, t_{95}^* increases more rapidly with t_2^* in the former case. This effect can be attributed to the slower rate of decay for dissolution in the shutdown regime when the shutdown regime is of sequential type.

Chapter 5

Unsteady source

Up until now, we have assumed a steady source having a buoyancy and mass flux that is time-invariant. In industrial practice, there are many instances where, by contrast, the source is unsteady, e.g. with alternating periods of activity and inactivity. Here we explore the associated dynamics with a particular emphasis on the evolution (and disappearance) of the gravity current post-injection, i.e. after the source has been "switched off". We therefore examine the spreading, draining and dissolution dynamics for $t^* > t_{\text{inj}}^*$ where t_{inj}^* is the (non-dimensional) time over which the source supplies contained fluid at a non-zero rate. When $t^* > t_{\text{inj}}^*$, influx boundary conditions specified by (3.21) must be modified such that the equations become homogeneous with zero right-hand side. More precisely, and whether $t \leq t_{\text{inj}}^*$ or $t > t_{\text{inj}}^*$, (3.21) is rewritten as

$$\left(h^* \frac{\partial h^*}{\partial x^*} \cos\theta + h^* \sin\theta \right)\Big|_{0^-} = -\mathrm{H}(t_{\text{inj}}^* - t^*)(1 - f_a)(1 - \delta h_{0^-}^* \cos\theta)^{\frac{1}{2}}$$

$$(5.1)$$

$$\left(h^* \frac{\partial h^*}{\partial x^*} \cos\theta - h^* \sin\theta \right)\Big|_{0^+} = -\mathrm{H}(t_{\text{inj}}^* - t^*) f_a (1 - \delta h_{0^+}^* \cos\theta)^{\frac{1}{2}}$$

Here H denotes the Heaviside step function.

Referencing (5.1), figure 5.1 shows the temporal evolution of the gravity current nose for simultaneous shutdown vs. sequential shutdown. In contrast to our previous analysis, here we select a comparatively small value of $t_2^* = 10$
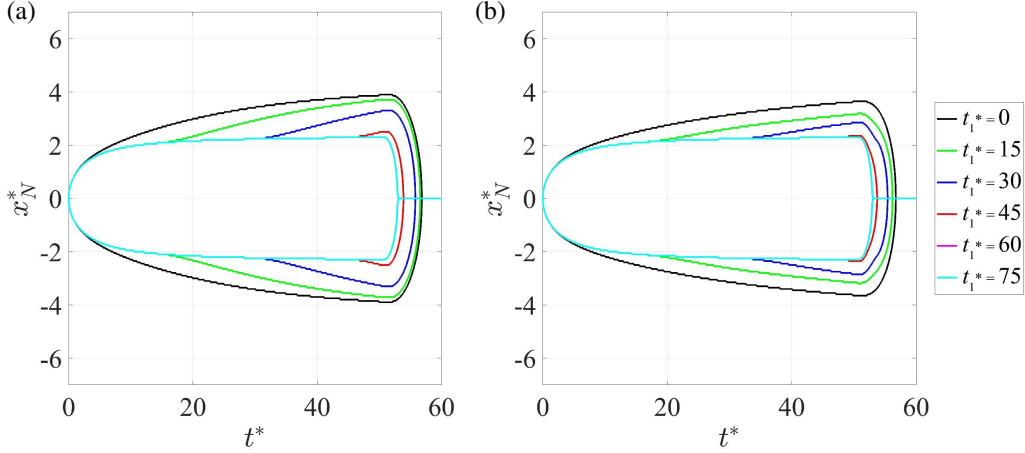
Figure 5.1: [Color online] Nose positions for $t^*_{\text{inj}} = 50$, $\theta = 0°$, $p = 1$, $t^*_2 = 10$ and various values of t^*_1. (a) Simultaneous shutdown and (b) sequential shutdown.

so as to better highlight the flow behavior in the period post-injection during which the gravity current is observed to recede relatively quickly. In like fashion, we likewise select relatively modest values for t^*_1. Figure 5.1 exhibits similar overarching behavior in either panel, i.e. for $t^* < t^*_{\text{inj}}$, the gravity current front advances quickly at first, then slows as intermediate run-out is approached. For $t^*_1 \leq 45$, intermediate run-out is followed by a remobilization of the gravity current front. However, once $t^* = t^*_{\text{inj}} = 50$, the source is switched off and no new contaminated fluid is supplied to the back of the gravity current. So although the front may travel some small additional distance downstream for t^* just larger than t^*_{inj}, there follows a period of rapid recession driven primarily by basal draining. In turn, the gravity current rapidly depletes from the upper layer. For example, and assuming $t^*_1 = 0$ for simultaneous shutdown, no contaminated fluid remains for $t^* > t^*_f = 56.84$ where t^*_f indicates the time required for the complete disappearance of contaminated fluid from the upper layer (except in dissolved form). At the opposite end of

54

the t_1^* spectrum, note that both x_N^* curves collapse when $t_1^* > t_{\text{inj}}^*$ in which case the gravity current begins to recede before the flow ever exits intermediate run-out.

Consistent with the above discussion, the time interval between t_{inj}^* and the instant where x_N^* achieves its maximum value is, owing to the limited inertia of the flow, comparatively small. This observation is especially true for large t_1^* where the maximum value of x_N^* is likewise small. In a similar spirit, the time, $t_f^* - t_{\text{inj}}^*$, required for gravity current fluid to disappear after the source is switched off is also small when t_1^* is large.

Comparing the left- and right- panels of figure 5.1, we find that gravity current remobilization evolves at a more leisurely pace when the dissolution mode is sequential in which case gravity currents tend not to propagate as far. Hence curves of x_N^* start at comparatively lower maximum values than do the counterpart curves corresponding to simultaneous shutdown. By repeating the analysis leading to figure 5.1 for other values of t_{inj}^* (not shown), we find that differences between the sequential and simultaneous shutdown regimes are more pronounced for smaller t_{inj}^*. When, by contrast, t_{inj}^* is large such that terminal run-out is approached, gravity current recession occurs in a nearly identical manner for the two different modes of shutdown.

So as to further highlight similarities and differences between the two different shutdown regimes in the context of t_{inj}^*, figure 5.2 shows surface plots of $t_f^* - t_{\text{inj}}^*$. Increasing the injection time increases the time to fully drain. Although this observation applies to both simultaneous and sequential dissolution, it is slightly more pronounced in the former. For sequential shutdown, incomplete shutdown means that comparatively less time is required for the gravity current fluid to disappear from the upper layer. When t_{inj}^* comfortably exceeds t_1^*, a terminal run-out plateau is approached, and differences between the left- and right-hand side surfaces decrease. The surface plots of figure 5.2

exhibit a second (low-level) plateau where $t_1^* \geq t_{\text{inj}}^*$: with short injection times, the gravity current drains completely into the lower layer before the onset of shutdown. In such a scenario, differences between simultaneous vs. sequential shutdown again disappear.

Whereas figures 5.2 a,b consider a flat permeability jump, figures 5.2 c,d assume instead $\theta = 10°$. Although strong qualitative similarities are evident in comparing figures 15 a,c and figures 5.2 b,d, we note that $t_f^* - t_{\text{inj}}^*$ values are typically smaller when the permeability jump is inclined. When $\theta > 0°$, a greater fraction of the source fluid is directed downdip, i.e. in an elongated gravity current whose thickness is less than when the permeability jump is horizontal. Correspondingly, and once the source is switched off, it takes less time for this gravity current fluid to disappear, either by dissolution or by draining into the lower layer.

The high- and low-level plateaus observed in figure 5.2 are reproduced in figure 5.3, which shows surface plots of $x_{N\text{max}}^*$, the maximum distance traversed by the gravity current nose. Not surprisingly, we find from figures 5.2 and 5.3 that parametric combinations that yield large $t_f^* - t_{\text{inj}}^*$ are also associated with large values for $x_{N\text{max}}^*$. Thus $x_{N\text{max}}^*$ is comparatively large when t_1^* is small in which case shutdown is realized early on and the gravity current has the opportunity to elongate following intermediate run-out. Furthermore, and as expected, $x_{N\text{max}}^*$ is large when source fluid is supplied for a long time such that t_{inj}^* is large.

Analogous to figures 5.2 c,d, the last four panels of figure 5.3 show, for $\theta = 10°$, the maximum extent of the gravity current in either the down- ($x_{N\text{max},d}^*$, panels c, d) or updip ($x_{N\text{max},u}^*$, panels e, f) directions. For both dissolution modes, we find that $x_{N\text{max},u}^* < x_{N\text{max}}^* < x_{N\text{max},d}^*$. Note also that, in the case of $x_{N\text{max},u}^*$, there exists a comparatively broad high-level plateau, particularly for simultaneous shutdown: on the updip side, the gravity current
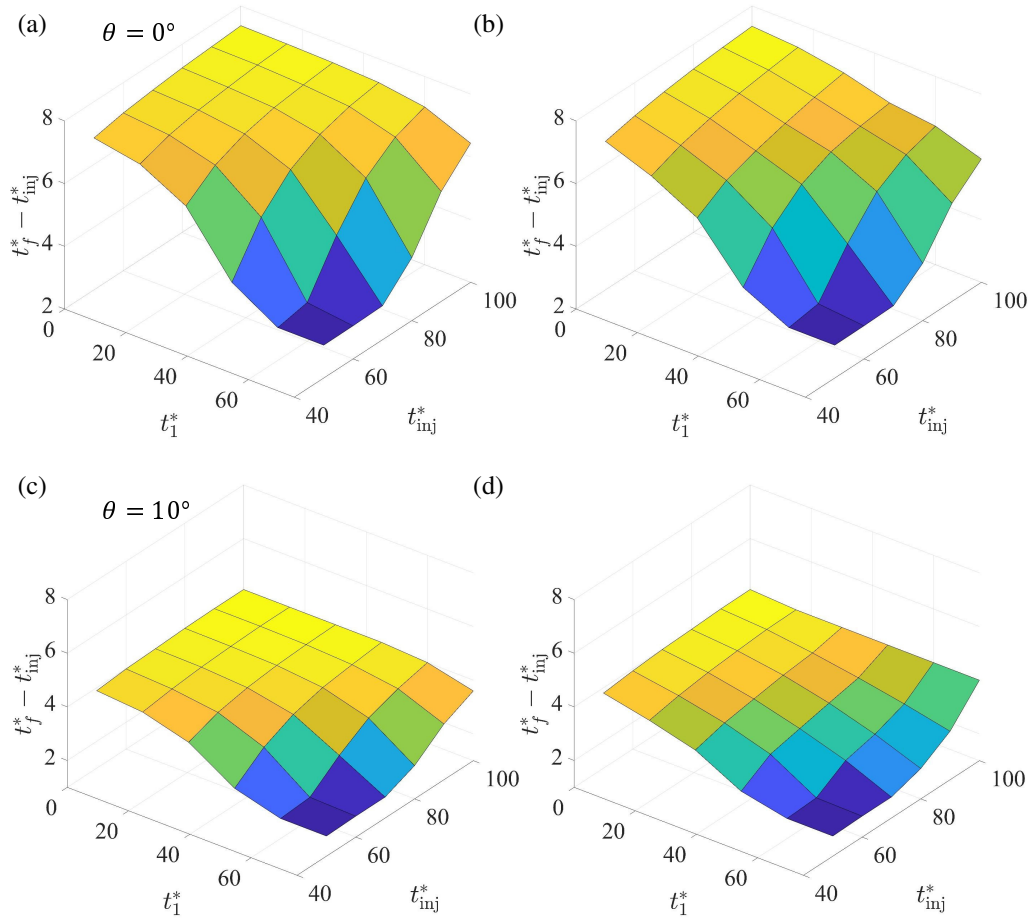
Figure 5.2: [Color online] Time, $t_f^* - t_{\mathrm{inj}}^*$, taken for gravity current fluid to completely disappear following the injection period as a function of t_1^* and t_{inj}^* with $p = 1$, $t_2^* = 10$. (a,c) Simultaneous shutdown and (b,d) sequential shutdown. The top row of panels show the case of a horizontal permeability jump while the bottom row of panels show $\theta = 10°$.
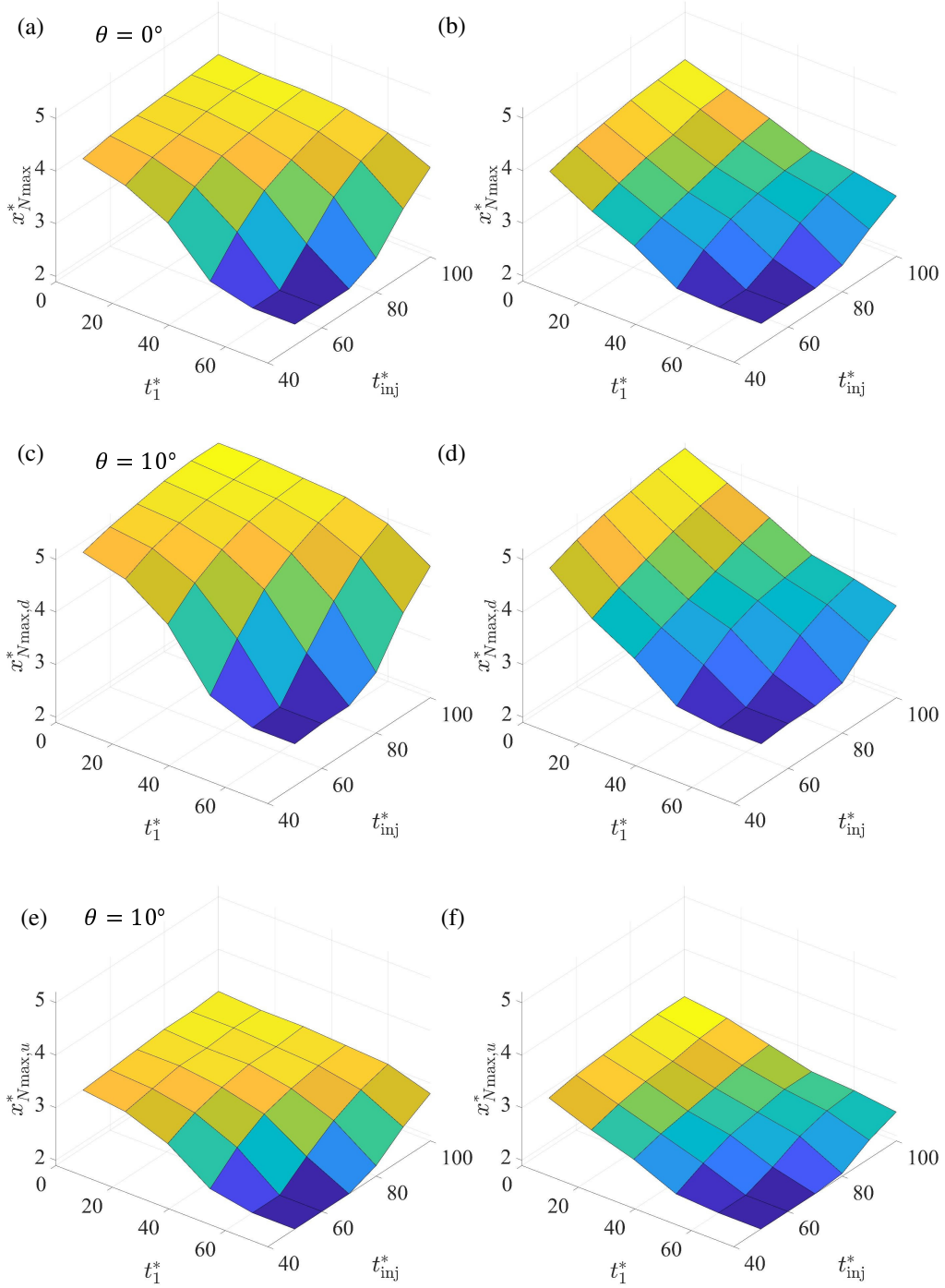
Figure 5.3: [Color online] Maximum along-jump distance traversed by the gravity current nose as a function of t_1^* and t_{inj}^* for $p = 1$, $t_2^* = 10$. (a,c,e) Simultaneous shutdown and (b,d,f) sequential shutdown. The top row shows the case of a horizontal permeability jump while the bottom four panels consider $\theta = 10°$.

front often becomes arrested well before $t^* = t^*_{\mathrm{inj}}$ due to the retarding influence of gravity. No such impediment exists on the downdip side, of course, and so the high-level plateau of figure 5.3 c is, by comparison, smaller than that observed in either of figures 5.3 a or, more especially, e.

Chapter 6

Solution bounds

In chapter 1, we remarked that sequential and simultaneous shutdown represent idealizations and that the true convective dissolution behavior must lie somewhere in between these limiting cases. It is necessary, therefore, to identify those regions of the parameter space where the bounds imposed by the simultaneous vs. sequential solutions are tight vs. loose. Such is the purpose of this section.

We begin by reexamining the steady source analysis of chapter 4 and use as the key variable of reference t_{95}^*, which is defined in figures 4.8 and 4.12. Synthesizing data from figure 4.8, we show in figure 6.1a the difference, Δt_{95}^*, of t_{95}^* values for the sequential case vs. the simultaneous case. Where Δt_{95}^* is small, the bound imposed by our previous analysis is tight. From the surface plot of figure 6.1a we observe that, for prescribed θ, the sequential and simultaneous solutions show greater differences when t_1^* is large and the onset of terminal run-out is delayed. This is the range of parameter space where the sequential shutdown mode exhibits the most pronounced stop-start behavior, a pattern of advance that is absent for simultaneous shutdown (see figures 4.5, 4.6, 4.9 and 4.10).

Similar to figure 6.1a, figure 6.1b shows Δt_{95}^* as a function of t_2^* and θ. Consistent with figure 6.1 a and the variation of Δt_{95}^* with t_1^*, we find from
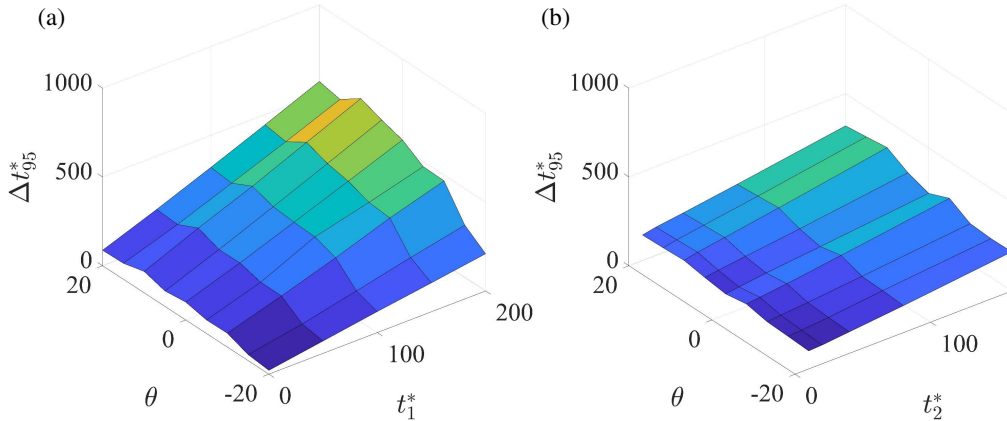
Figure 6.1: [Color online] Difference of t_{95}^* values for sequential vs. simultaneous shutdown. (a) Δt_{95}^* vs. θ and t_1^* for $t_2^* = 50$, (b) Δt_{95}^* vs. θ and t_2^* for $t_1^* = 50$. The angle θ is measured in degrees.

figure 6.1 b that Δt_{95}^* likewise increases with t_2^*, small t_2^* being associated with pronounced stop-start behavior in the case of sequential shutdown.

Figure 18 shows a similar kind of comparison but with reference to an unsteady source and $x_{N\mathrm{max}}^*$ rather than t_{95}^*. From figure 6.2 a, we observe that $\Delta x_{N\mathrm{max}}^*$ is small in two opposite limits: large t_1^*/small t_{inj}^* and small t_1^*/large t_{inj}^*. In the former case and consistent with figure 5.1, the source is switched off before the onset of shutdown. Consequently, the flow remains in a state of intermediate run-out such that there is no difference between the simultaneous vs. sequential regimes. In the opposite limit of small t_1^*/large t_{inj}^*, the dissolution rate begins to fall almost immediately and there is ample opportunity for the gravity currents to approach terminal run-out. Although this limit admits some differences between simultaneous vs. sequential dissolution, these differences are small and likewise the values of $\Delta x_{N\mathrm{max}}^*$. In between the large t_1^*/small t_{inj}^* and small t_1^*/large t_{inj}^* limits, the flow lies between intermediate and terminal run-out and the two dissolution modes admit more significant differences given that gravity current fluid travels greater horizontal distances

61
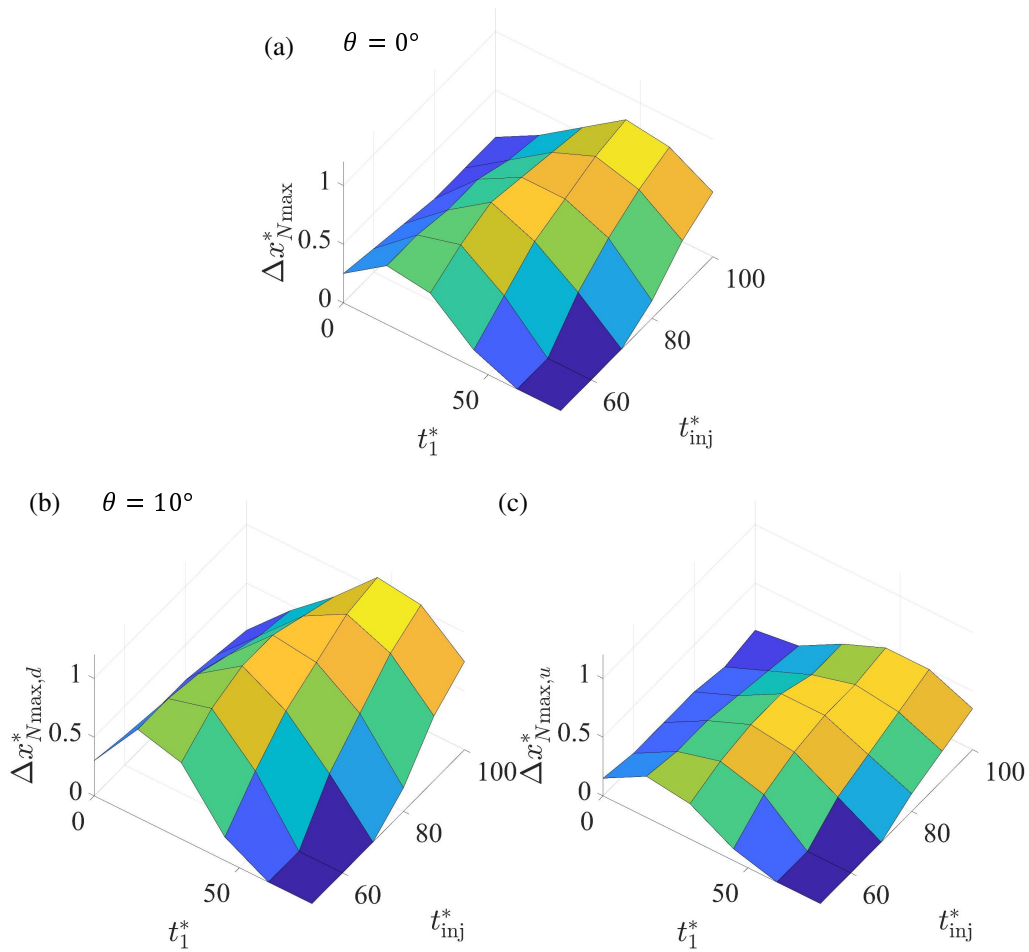
Figure 6.2: [Color online] Difference in the maximum nose position, $\Delta x^*_{N\max}$, between sequential and simultaneous shutdown for (a) $\theta = 0°$ and $p = 1$. The bottom row of panels correspond to $\theta = 10°$ and (b) downdip flow, $\Delta x^*_{N\max,d}$. and (c) updip flow, $\Delta x^*_{N\max,u}$.

along the permeability jump when the shutdown mode is simultaneous.

Similar to figure 6.2 a, figure 6.2 b,c respectively indicate $x^*_{N\mathrm{max}}$ in the down- and updip directions for $\theta = 10°$. In the downdip direction, the gravity current speed increases with θ, which has the effect of amplifying the trends documented in figure 6.2 a. By comparison, we expect the aforementioned trends to be subdued when considering the updip direction for which gravity retards the forward advance of the flow. Figure 6.2 c confirms this expectation.

Chapter 7

Conclusions, Recommendations and Future Work

7.1 Conclusions

In the present study, we superpose convective dissolution instabilities on the advancing front of a gravity current that propagates along the permeability jump between a high permeability upper layer and a low permeability lower layer. The permeability jump makes an angle θ to the horizontal and the upper layer is, except for the analysis of section 4.1, considered to be finite in vertical extent. The primary contribution of this investigation is to incorporate convective dissolution into a mathematical model that describes, in a sharp-interface, large Bond number framework, the spatio-temporal evolution of a plume-fed, leaky gravity current. We consider dissolution rates that are either constant (section 4.1) or time-variable (section 4.2 and section 4.3). In the latter case, section 4.2 considers a scenario where the lateral mixing of contaminated fluid within the ambient is relatively rapid; thus the dissolution rate is everywhere the same along the gravity current length. We refer to this case as "simultaneous shutdown." By contrast, section 4.3 considers the bookend opposite scenario where lateral mixing within the ambient is slow such that different segments of the gravity current experience dissolution shutdown at different instants in time. We refer to this case as "sequential shutdown."

Neither of the scenarios just described is a true representation of the dissolution process, however, they provide helpful limiting cases that bound the true behavior of the system under investigation. In either case, dissolution is parameterized with reference to variables t_1^* and t_2^*, which respectively represent the non-dimensional time for which the dissolution rate is constant and the e-folding decay time in the shutdown regime – see figure 1.2.

Of key interest in this study is to explore the up- and downdip gravity current evolution as a function of θ, t_1^*, t_2^* and the dissolution strength, p. To this end, we show the time evolution of the gravity current shape (figure 4.1), nose position (figures 4.2, 4.5 and 4.9), downdip flow fraction (figures 4.2, 4.6 and 4.10) and storage efficiency (figure 4.2, 4.7 and 4.11). We also characterize, in figures 4.8 and 4.12, the time, t_{95}^*, required to reach 95% of the terminal run-out length. On the basis of the results just described, a number of significant conclusions follow. For constant dissolution, p plays a significant role in limiting the maximum extent of the gravity current, both up- and downdip. Stated differently, the arrest of the along jump migration is most prominent for small p, which signifies strong dissolution. In other words, small p is associated with short run-out times and lengths and also with large storage efficiencies.

Solutions from the simultaneous vs. sequential shutdown models demonstrate that once the dissolution rate begins to fall, the balance between dissolution, draining and plume inflow is disrupted such that previously-arrested gravity current fronts may remobilize. Up- and downdip propagation therefore resumes until such time as the rate of plume inflow matches the rate of basal draining. Only then is terminal run-out is realized. The stop-start motion just described is reminescent of that described in Bharath et al. (2020). In that paper, the authors consider a lower, rather than an upper layer, of finite depth. As a consequence, a secondary gravity current is generated once the

draining fluid comes into contact with an impermeable bottom boundary. This secondary gravity current ultimately "tugs" upon the previously-arrested primary gravity current, causing it to resume its up- and downdip propagation. On the other hand, and whereas the along-jump gravity current is arrested at most one time in the study of Bharath et al. (2020), sequential shutdown offers richer dynamical behavior, at least in the limit of large t_1^* or small t_2^*. More precisely, several intermediate stops of the gravity current front are witnessed during the remobilization phase.

Considering the impact of t_2^*, a decrease in t_2^* increases the aggressiveness of remobilization and increases the degree of up- vs. downdip flow asymmetry, an effect that is especially prominent for simultaneous shutdown. In the case of sequential shutdown, the start stop motions become prominent for small t_2^*.

In the case of an unsteady sourse, the gravity currently rapidly recedes and ultimately disappears from the upper layer following an injection period, t_{inj}^*. Further, the maximum nose distance, $x_{N\text{max}}^*$ and the time, $t_f^* - t_{\text{inj}}^*$ taken to fully drain following the injection period increases rapidly as t_1^* is decreased. This effect is somewhat suppressed for sequential shutdown on account of residual dissolution experienced for $t^* > t_{\text{inj}}^*$. Comparing the regions of the parameter space where simultaneous and sequential shutdown yield comparable predictions, we such similarities in the opposing limits of large t_1^*/small t_{inj}^* and small t_1^*/large t_{inj}^*. Consistent with the steady source scenario, the solutions from the simultaneous shutdown and sequential shutdown models are similar for small t_1^* but begin to diverge as t_1^* increases owning chiefly to the more leisurely remobilization speed experienced for sequential shutdown.

7.2 Primary Contributions from the Present Work

The primary findings of this thesis can be highlighted below with the following points:

- We have successfully superimposed into the governing equation for buoyancy driven flow in a two layered porous medium a term describing transient convective dissolution, where the concentration of the gravity current fluid being dissolved into the ambient varies with time nonlinearly. In contrast to previous studies that consider an impermeable top seal (MacMinn and Juanes 2013; Szulczewski et al. 2013; MacMinn et al. 2011), the incorporation of a less permeable lower layer in addition to the retention effects of dissolution leads to more nuanced and complicated dynamics. Stated differently, dissolution provides a means for the discharged plume fluid to remain permanently dissolved and build up in the upper layer until the point of where it's fully saturated. We have analyzed and investigated the nuanced interplay between advection, dissolution and draining in this setting in both the short and the long term limit. For shallow layers, short term equilibrium is reached when source influx equals draining and dissolution. The time after which dissolution fails to remain constant and its rate starts to diminish, a remobilization of the previously arrested front is observed which in the long-term limit establishes a secondary equilibrium point where source influx balances draining only. Whereas in Bharath et al. (2020), remobilization is achieved once the draining draining fluid strikes an impermeable bottom boundary, re-mobilization in this thesis is manifested as a result of the diminishing rate of dissolution owning to the gradual saturation of the upper layer with contaminated fluid.

- Using simple analytical models of convective dissolution, we have demonstrated that the up- and downdip migration of the gravity current is significantly curtailed in the case of strong dissolution. Considering a steady source in a two layer porous medium with the upper layer having an infinite depth, a significant increase in storage efficiency is observed as the dissolution strength increases. Thus the long term fate of the injectate will be not be a cause for concern as the injectate will remain permanently sequestered under such conditions. The interplay between advection, draining and dissolution is quantified in the sense that at the point of terminal run-out in these deep aquifers, the gravity current stops advecting as source influx equals the flux losses associated with draining and dissolution. Also to note is that the aquifer slope only marginally alters the storage efficiency in these cases chiefly because the exposed interface subjected to dissolution has a total area that varies little with the tilt angle, θ. The time taken to reach terminal runout is primarily a function of the dissolution strength. As the dissolution strength increases, the time taken for the gravity current to become fully arrested falls. Our findings reveal that deeper formations are far superior in retaining injected contaminants than shallower formations/aquifers and that the value of the inclination angle of abrupt permeability changes in these strata is largely immaterial considering a long term injected period.

- By bounding all flow possibilities within two extremes, namely dissolution with simultaneous and sequential shutdown in the case of a finite upper layer, we have quantitatively highlighted regions of the parameter space where similar solutions from both regimes of dissolution can be enjoyed. In considering the theoretical models utilized here, the order one predictions about the spreading dynamics in conjunction with ex-

periments performed in a Hele-Shaw or layers can provide insights into real sequestration flows. Our models have laid sufficient groundwork for designing complex experiments with two layers to include vertical plume migration combined with lateral movement along a permeability jump with dissolution. If measurements made in the laboratory supported the predictions of the current theoretical model, one would have even greater confidence in extrapolating model output to field-scale engineering flows. Once this is achieved, predictions from these simple models may be incorporated through parameterization into more computationally demanding computer algorithms.

- We have identified that for finite injection periods, an additional recession zone occurs after the source is switched off. This region of rapid backwards movement exists for short time scales and so serves to eliminate the gravity current. Where mixing between the gravity current and ambient occurs only in the vertical direction (sequential shutdown), the recession velocities are low and thus the gravity current enjoys a comparatively larger amount of time in the upper layer before being completely drained into the lower layer.

- For shallow aquifers, the effectiveness of dissolution is largely limited by its depth and its retentiveness for the discharged plume fluid that is trapped by dissolution. If the upper cap rock seal is less permeable than what is considered in the inverted geometry of this study, the gravity current will be able to travel further distances, specifically updip along the permeability jump and thus be able to cover a more expansive area. Although this might open up possibilities for leakages through isolated fissures or cracks, the larger migration distance will expose the current to more groundwater, thereby increasing the amount of fluid dissolved

by dissolution.

7.3 Future Work

A few topics that can be tackled in future are as follows:

- In the present study, we have considered a zero entrainment condition for the draining fluid. In doing so, we have set $G' = 1$ in the governing equation 3.4 for the gravity current height. This variable plays a non-trivial role in determining the up- and downdip run-out lengths atop the permeability jump. Specifically, G' dictates the degree of ambient fluid entering the draining fluid as it descends further into the lower layer of the porous formation. In recent work by Bharath et al. (2020), a value of $G' < 1$ is used to indicate a gradual thickening of the draining fluid as it engulfs fresh ambient fluid in its descent. Indeed, experiments conducted by the authors reveal that there exists an empirical relationship between G' and the plume source parameters. Incorporating the empirical relationship into the existing theoretical models or developing a theoretical relationship between said independent source parameters and G' might unveil further insights into the true nature of the flow and thus remains to be investigated.

- In chapter 3, we have incorporated into the governing equation for gravity current thickness, a convective instability without taking into account the effects caused by residual trapping and eventual long-term mineralization. The key assumption for ignoring residual trapping here is that the capillary forces are small compared to gravitational and viscous forces. Although, the mineralization is associated with extremely large timescales that will not be suited for numerical simulation of short term injection, capillary effects can be combined in the existing model

using either a constant term such as the volumetric fraction of residual gas trapping or other time varying parameters that rely on relative saturation (Goda and Sato 2011). The parameter associated with the volumetric fraction of residual gas trapping when included will appear in the partial differential equations for solving h^* and l^*. This will lead, in the associated solutions, to the formation of a receding interface of the trapped fluid in the evolution of the plume profile, simulating bubbles of CO_2 trapped as ganglia in the pore spaces of the reservoir formation. Some additional factors that can be considered to add to the complexity of the numerical model will include surface tension, capillary pressure and as previously mentioned the relative amount of pore saturation. The superposition of such effects will lead to the development of a multiphase flow model that can predict the fluid retained in the injection layer as a result of residual trapping, with additional retention caused by convective dissolution (MacMinn et al. 2011; Bickle 2009).

- Although fingering instabilities associated with vigorous dissolution have not been explicitly considered in the present investigation, a challenge still remains in modelling their occurrence in configurations where hydrodynamics instabilities might be large enough to trigger such phenomena. The fingers are visible in experiments conducted by MacMinn and Juanes (2013) and Szulczewski et al. (2013), and appear shortly after the onset of early diffusion. A straightforward approach can involve segmenting the shutdown regime into its respective stages consistent with Szulczewski et al. (2013). Thus the third region of 3.20 can be modified to implement each phase of shutdown as it appears in trials conducted in a Hele-Shaw cell. Thus preliminary forays into this study will lead to the development of semi-empirical equations of the various shutdown

regimes namely: shutdown/fingering, shutdown/slumping, shutdown/-Taylor slumping, Taylor slumping and finally late diffusion which results in near perfect saturation.

- Complementary to the theoretical investigation conducted in the present study, a series of experiments can be carried out using fresh water as the primary plume fluid with the ambient fluid being either propylene glycol (MacMinn and Juanes 2013) or ethylene glycol and methanol (Neufeld et al. 2010) mixed together. Noting the experimental limitations from Raad and Hassanzadeh (2017), a large viscosity ratio between the ambient and plume fluid is required to trigger convective dissolution in a system that is initially stably stratified, which fits nicely with the chosen fluid mentioned above. In the case of glycerol and water as the ambient fluid, mixing between the ambient and plume fluid is only by a process of dispersion and diffusion, which does not drive convective dissolution (MacMinn et al. 2011). We expect that in such a system, the buoyant plume of fresh water will rise through the viscous glycol ambient whilst simultaneously being being dissolved in it leading to dense fingers of water rich glycol trickling down to the bottom of the testing cell. By tracking the nose position of the gravity current using shadowgraphy and measuring the nose's front speed, the analytical model developed here can be validated.

Bibliography

Lüthi, D., Le Floch, M., Bereiter, B., Blunier, T., Barnola, J.-M., Siegenthaler, U., Raynaud, D., Jouzel, J., Fischer, H., Kawamura, K. et al. (2008). High-resolution carbon dioxide concentration record 650,000–800,000 years before present. *nature*, *453*(7193), 379–382.

Huppert, H. E., & Neufeld, J. A. (2014). The fluid mechanics of carbon dioxide sequestration. *Annu. Rev. Fluid Mech.*, *46*, 255–272. https://doi.org/10.1146/annurev-fluid-011212-140627

Khalil, M., & Shearer, M. (2000). Sources of methane: An overview. *Atmospheric Methane*, 98–111.

Tiseo, I. (n.d.). *Annual co_2 emissions worldwide from 1940 to 2020.* https://www.statista.com/statistics/276629/global-co2-emissions/ (accessed: 01.23.2022)

Essenhigh, R. H. (2009). Potential dependence of global warming on the residence time (rt) in the atmosphere of anthropogenically sourced carbon dioxide. *Energy & Fuels*, *23*(5), 2773–2784.

Keith, D. W. (2000). Geoengineering the climate: History and prospect. *Annual review of energy and the environment*, *25*(1), 245–284.

Allen, M., Babiker, M., Chen, Y., & de Coninck, H. C. (2018). Ipcc sr15: Summary for policymakers. *IPCC Special Report Global Warming of 1.5 ºC.*

Nordbotten, J. M., Celia, M. A., Bachu, S., & Dahle, H. K. (2005). Semianalytical solution for co2 leakage through an abandoned well. *Environmental science & technology*, *39*(2), 602–611.

Ide, S. T., Jessen, K., & Orr Jr, F. M. (2007). Storage of co2 in saline aquifers: Effects of gravity, viscous, and capillary forces on amount and timing of trapping. *International Journal of Greenhouse Gas Control*, *1*(4), 481–491.

Kochina, I., Mikhailov, N., & Filinov, M. (1983). Groundwater mound damping. *International Journal of Engineering Science*, *21*(4), 413–421.

Qi, R., LaForce, T. C., & Blunt, M. J. (2009). Design of carbon dioxide storage in aquifers. *International Journal of Greenhouse Gas Control*, *3*(2), 195–205.

Zoback, M. D., & Gorelick, S. M. (2012). Earthquake triggering and large-scale geologic storage of carbon dioxide. *Proceedings of the National Academy of Sciences*, *109*(26), 10164–10168.

Rinaldi, A. P., Vilarrasa, V., Rutqvist, J., & Cappa, F. (2015). Fault reactivation during co2 sequestration: Effects of well orientation on seismicity and leakage. *Greenhouse Gases: Science and Technology*, *5*(5), 645–656.

Leonenko, Y., & Keith, D. W. (2008). Reservoir engineering to accelerate the dissolution of co2 stored in aquifers. *Environmental science & technology*, *42*(8), 2742–2747.

Nordbotten, J. M., & Celia, M. A. (2006). Similarity solutions for fluid injection into confined aquifers. *J. Fluid Mech.*, *561*, 307–327. https://doi.org/10.1017/S0022112006000802

Zhao, W., & Ioannidis, M. A. (2007). Convective mass transfer across fluid interfaces in straight angular pores. *Transport in porous media*, *66*(3), 495–509.

Pritchard, D. (2007). Gravity currents over fractured substrates in a porous medium. *J. Fluid Mech.*, *584*, 415–431. https://doi.org/10.1017/S0022112007006623

Goda, T., & Sato, K. (2011). Gravity currents of carbon dioxide with residual gas trapping in a two-layered porous medium. *J. Fluid Mech.*, *673*, 60–79. https://doi.org/10.1017/S0022112010006178

Sahu, C. K., & Flynn, M. R. (2015). Filling box flows in porous media. *J. Fluid Mech.*, *782*, 455–478.

Bharath, K. S., Sahu, C. K., & Flynn, M. R. (2020). Isolated buoyant convection in a two-layered porous medium with an inclined permeability jump. *J. Fluid Mech.*, *902*, A22. https://doi.org/10.1017/jfm.2020.599

Bharath, K. S., & Flynn, M. R. (2021). Buoyant convection in heterogeneous porous media with an inclined permeability jump: An experimental investigation of filling box-type flows. *J. Fluid Mech.*, *924*. https://doi.org/10.1017/jfm.2021.542

MacMinn, C. W., & Juanes, R. (2013). Buoyant currents arrested by convective dissolution. *Geophys. Res. Lett.*, *40*(10), 2017–2022. https://doi.org/10.1002/grl.50473

Szulczewski, M. L., Hesse, M. A., & Juanes, R. (2013). Carbon dioxide dissolution in structural and stratigraphic traps. *J. Fluid Mech.*, *736*, 287–315. https://doi.org/10.1017/jfm.2013.511

MacMinn, C. W., Szulczewski, M. L., & Juanes, R. (2011). CO_2 migration in saline aquifers. Part 2. Capillary and solubility trapping. *J. Fluid Mech.*, *688*, 321–351.

Huppert, H. E., & Woods, A. W. (1995). Gravity-Driven Flows in Porous Layers. *J. Fluid Mech.*, *292*, 55–69. https://doi.org/10.1017/S0022112095001431

Vella, D., & Huppert, H. E. (2006). Gravity currents in a porous medium at an inclined plane. *J. Fluid Mech.*, *555*(1992), 353–362. https://doi.org/10.1017/S0022112006009578

Lyle, S., Huppert, H. E., Hallworth, M., Bicle, M., & Chadwick, A. (2005). Axisymmetric gravity currents in a porous medium. *J. Fluid Mech.*, *543*(2005), 293–302. https://doi.org/10.1017/S0022112005006713

Bolster, D. (2014). The fluid mechanics of dissolution trapping in geologic storage of CO_2. *J. Fluid Mech.*, *740*, 1–4. https://doi.org/10.1017/jfm.2013.531

Bear, J. (1988). *Dynamics of fluids in porous media*. Courier Corporation.

Phillips, O. M. (1991). *Flow and reactions in permeable rocks*. Cambridge University Press.

Dullien, F. A. (2012). *Porous media: Fluid transport and pore structure*. Academic press.

Rumpf, H, & Gupte, A. (1975). The influence of porosity and grain size distribution on the permeability equation of porous flow. *NASA STI/Recon Technical Report N*, *43*(6), 367–375.

Farcas, A., & Woods, A. W. (2013a). Three-dimensional buoyancy-driven flow along a fractured boundary. *Journal of fluid mechanics*, *728*, 279–305.

Neufeld, J. A., Vella, D., & Huppert, H. E. (2009). The effect of a fissure on storage in a porous medium. *Journal of fluid mechanics*, *639*, 239–259.

Neufeld, J. A., Vella, D., Huppert, H. E., & Lister, J. R. (2011). Leakage from gravity currents in a porous medium. part 1. a localized sink. *Journal of Fluid Mechanics*, *666*, 391–413.

Pritchard, D., Woods, A. W., & Hogg, A. J. (2001). On the slow draining of a gravity current moving through a layered permeable medium. *Journal of Fluid Mechanics*, *444*, 23–47.

Neufeld, J. A., & Huppert, H. E. (2009). Modelling carbon dioxide sequestration in layered strata. *Journal of Fluid Mechanics*, *625*, 353–370.

Woods, A. W., & Farcas, A. (2009). Capillary entry pressure and the leakage of gravity currents through a sloping layered permeable rock. *Journal of fluid mechanics*, *618*, 361–379.

Yu, Y. E., Zheng, Z., & Stone, H. A. (2017). Flow of a gravity current in a porous medium accounting for drainage from a permeable substrate and an edge. *Physical Review Fluids*, *2*(7), 074101.

Farcas, A., & Woods, A. W. (2013b). Three-dimensional buoyancy-driven flow along a fractured boundary. *Journal of fluid mechanics*, *728*, 279–305.

De Loubens, R, & Ramakrishnan, T. (2011). Analysis and computation of gravity-induced migration in porous media. *Journal of fluid mechanics*, *675*, 60–86.

Farcas, A., & Woods, A. W. (2009). The effect of drainage on the capillary retention of co2 in a layered permeable rock. *Journal of fluid mechanics*, *618*, 349–359.

Cowton, L., Neufeld, J., White, N., Bickle, M., White, J., & Chadwick, R. (2016). An inverse method for estimating thickness and volume with time of a thin co2-filled layer at the sleipner field, north sea. *Journal of Geophysical Research: Solid Earth*, *121*(7), 5068–5085.

Hewitt, D. R., Peng, G. G., & Lister, J. R. (2020). Buoyancy-driven plumes in a layered porous medium. *Journal of Fluid Mechanics*, *883*.

Sahu, C. K., & Flynn, M. (2017). The effect of sudden permeability changes in porous media filling box flows. *Transport in Porous Media, 119*(1), 95–118.

Acton, J. M., Huppert, H. E., & Worster, M. G. (2001). Two-dimensional viscous gravity currents flowing over a deep porous medium. *Journal of fluid mechanics, 440*, 359–380.

Delgado, J. (2007). Longitudinal and transverse dispersion in porous media. *Chemical Engineering Research and Design, 85*(9), 1245–1252.

Zhang, Y., & Xu, Z. (2003). Kinetics of convective crystal dissolution and melting, with applications to methane hydrate dissolution and dissociation in seawater. *Earth and Planetary Science Letters, 213*(1-2), 133–148.

Hewitt, D. R., Neufeld, J. A., & Lister, J. R. (2013). Convective shutdown in a porous medium at high rayleigh number. *Journal of Fluid Mechanics, 719*, 551–586.

Bickle, M. J. (2009). Geological carbon storage. *Nature Geoscience, 2*(12), 815–818.

Neufeld, J. A., Hesse, M. A., Riaz, A., Hallworth, M. A., Tchelepi, H. A., & Huppert, H. E. (2010). Convective dissolution of carbon dioxide in saline aquifers. *Geophysical research letters, 37*(22).

Raad, S. M. J., & Hassanzadeh, H. (2017). Prospect for storage of impure carbon dioxide streams in deep saline aquifers—a convective dissolution perspective. *International Journal of Greenhouse Gas Control, 63*, 350–355.